J. Mech. Phys. Solids 167 (2022) 104982

Contents lists available at ScienceDirect

Journal of the Mechanics and Physics of Solids

journal homepage: www.elsevier.com/locate/jmps

A mesoscale model for the micromechanical study of gels

Robert J. Wagner, Jinyue Dai [1], Xinfu Su [1], Franck J. Vernerey [*]

Department of Mechanical Engineering & Material Science and Engineering Program, University of Colorado at Boulder, Boulder 80309-0428, USA

ARTICLE INFO

Keywords:
Gels
Microstructures
Fracture mechanisms
Inhomogeneous material
Numerical algorithms

ABSTRACT

Gels are comprised of polymer networks swelled by some interstitial solvent. They are under wide investigation by material scientists and engineers for their broad applicability in fields ranging from adhesives to tissue engineering. Gels' mechanical properties greatly influence their efficacy in such applications and are largely dictated by their underlying microstructures and constituent-scale properties. Yet predictively mapping the local-to-global property functions of gels remains difficult due - in part - to the complexity introduced by solute-solvent interactions. We here introduce a novel, discrete mesoscale modeling method that preserves local solute concentration-dependent gradients in osmotic pressure through the Flory-Huggins mixing parameter, χ. The iteration of the model used here replicates gels fabricated from telechelically crosslinked star-shaped polymers and intakes χ, macromer molecular weight (M_w), crosslink functionality (f), and as-prepared solute concentration (ϕ^*) as its inputs, all of which are analogues to the control parameters of experimentalists. Here we demonstrate how this method captures solvent-dependent homogenization ($\chi \leq 0.5$) or phase separation ($\chi > 0.5$) of polymer suspensions in the absence of phenomenological pairwise potentials. We then demonstrate its accurate, *ab initio* prediction of gel topology, isotropic swelling mechanics, and uniaxial tensile stress for a 10k tetra-PEG gel. Finally, we use the model to predict trends in the mechanical response and failure of multi-functional PEG-based gels over a range of M_w and f, while investigating said trends' micromechanical origins. The model predicts that increased crosslink functionality results in higher initial chain stretch (as measured at the equilibrated swollen state) for gels of the same underlying chain length, which improves modulus and failure stress but decreases failure strain and toughness.

1. Introduction

Gels generally consists of a skeletal network of high molecular weight polymer chains interpenetrated by low molecular weight solvent. This two-state composition imparts gels with complex mechanical response that depends on the topological evolution of the skeleton, transport properties of the solvent, and the interactions between them. The entropic stiffness of the polymer network and time-dependent transport of fluid impart gels with elastic and poroelastic responses, respectively, while non-affine network deformation, entanglements, and the intrinsic viscosity of the solvent introduce various sources of viscous dissipation. Furthermore, inclusion of sacrificial bonds (Elbanna and Carlson, 2013; Fantner et al., 2005; Kothari et al., 2018; Lieou et al., 2013); bonds that break and reform without damage (Gianneli et al., 2007; Narita et al., 2013); or irreversible chain rupture (Sugimura et al., 2013) induce

* Corresponding author.
E-mail address: franck.vernerey@colorado.edu (F.J. Vernerey).
[1] These authors contributed equally to this work.

https://doi.org/10.1016/j.jmps.2022.104982
Received 15 February 2022; Received in revised form 18 May 2022; Accepted 8 June 2022
Available online 9 June 2022
0022-5096/

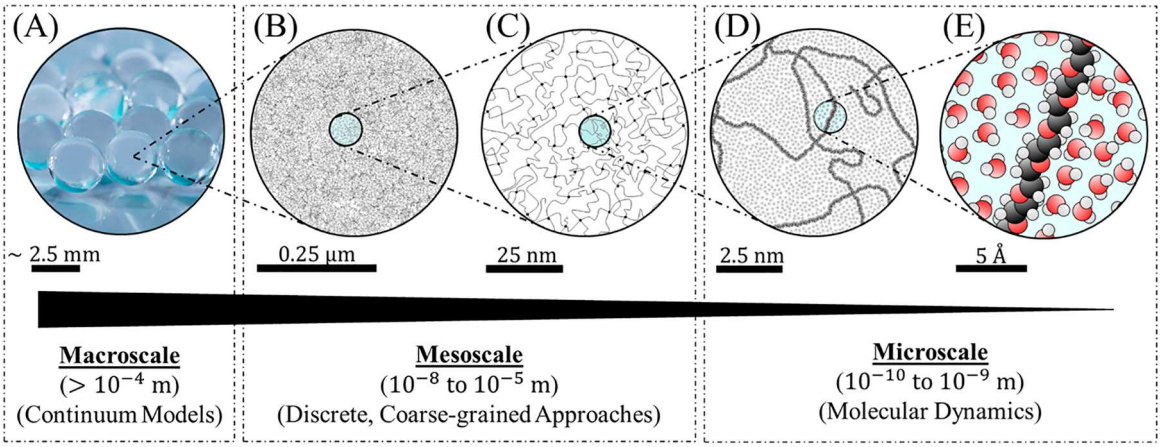

Fig. 1. Hierarchical length scales of gels. A gel at (A) the macroscale ($>\sim 10^{-4}$ m) is depicted with schematic illustrations of its topological structure at (B–E) diminishing length scales. (A) At the macroscale, smoothing assumptions permit application of continuum approaches, but these methods prohibit detailed study of damage or the influence of defects. (B,C) The discrete methods introduced here represent gel structures at intermediate length scales or the "mesoscale" by coarse-graining polymer chains as nonlinear mechanical springs. In modeling individual polymer chains, mesoscale approaches are equipped to capture the mechanical effects of topological defects and damaged regions, with reduced computational expense. (D-E) The most detailed models track constituents (either atoms, molecules, or Kuhn segments) utilizing discrete MD approaches. However, capturing defects on the order of 10^{1} nm to 10^{-1} μm, or conducting large ensembles of repeated *in silico* experiments becomes computationally untenable using these fine-grained approaches. The gel topology shown is meant to loosely represent a tetra-PEG hydrogel whose mesh size is on the order of 10^{-8} m and which has 4 functional arms per macromer.

topological evolution in gels that may improve toughness (Li et al., 2021, 2020), and introduce stress relaxation or self-healing (Long et al., 2014). These mechanical traits render gels especially suitable candidates in applications such as tissue engineering wherein they are often used as cell scaffolds (Richardson et al., 2019). In such applications, gels' moduli and stress relaxation rates influence stem cell differentiation and in-growth of new tissue (Chaudhuri et al., 2016; Choi et al., 2016; Yang et al., 2016). Thus, this exemplifies a case in which understanding the mechanical properties of a gel as a function of its fabrication parameters would greatly aid researchers. Indeed, modeling techniques that accurately predict the microstructural evolution and globally emergent mechanical properties of gels are highly sought after. However, the hierarchical structure of gels renders it difficult to formulate computationally tenable, non-phenomenological models that track topological changes in gels across length scales.

Gels are inherently multiscale materials, whose pertinent constituents (i.e., solvent particles and mers) are on the atomistic scale, yet whose characteristic chain and pore sizes are on the scale of nanometers (Matsunaga et al., 2009a) (Fig. 1). Furthermore, defects on the order of 10^{1}–10^{3} nm may exist in the network, which grow due to local stress concentrations. Understanding the emergence, evolution, and propagation of these defects, as well as their cause, is imperative to understanding the failure and strength of gels (Chen et al., 2017; Yang et al., 2019). These pore sizes and defects suffuse gels with intrinsic property gradients and heterogeneity at the network scale. The size of these features limits the resolution with which continuum approaches may be applied since such models typically invoke smoothing assumptions and require homogenous materials. However, the length scale of these features also ensures that within a representative element on the order of cubic micrometers, $10^{9} - 10^{12}$ constituents would need to be modeled in fine-grained approaches, thus also limiting the efficacy of methods such as molecular dynamics (MD) (Lange et al., 2011). As such, many MD studies focus on the interaction of just one or a few macromers (Huissmann et al., 2009; Johner and Lee, 2018; Jusufi et al., 1999). Even employing coarse-graining practices to MD, such as those of Wang and Escobedo (2017) (e.g., the use of Kuhn segments for bead-spring chains and smoothing of the solvent), such approaches require large computational time and resources. Therefore, a tertiary class of explicit, mesoscopic models are needed to bridge the microstructural-to-global mechanical property response of gels. Such approaches may capture the length scale of heterogeneities and local topological traits while leveraging statistical representations of features such as individual entropic chains or mixing effects.

Towards this aim, researchers such as Sugimura et al. (2013) have used mesoscale models to study the mechanics of gels. Indeed, these researchers and much of the existing literature have focused on perhaps the most idealized polymeric networks observed in gels to date - those of tetra-polyethylene glycol (PEG) based gels. In fact, such gels are under strong consideration in bioengineering applications for their biocompatibility and the ease with which their mechanical properties may be tuned. These networks are formed through the gelation of star-shaped macromers with functional arms that bind to one another telechelically (i.e., at their terminal ends), and achieve high conversion rates (Lange et al., 2011), with relatively few defects (Akagi et al., 2010) and high homogeneity (Matsunaga et al., 2009b, 2009a). The relative homogeneity of these networks has allowed researchers such as Sugimura et al. (2013) to initiate modeled gels as ideal diamond lattices from which bonds are stochastically and retroactively removed, while still accurately predicting their mechanical response. However, this phenomenological gelation approach is empirically motivated, and the correct topologies are set according to experimental results rather than emerging because of the underlying physics. As such, these idealized approaches are ill-suited to capture the local microstructures of gels with transient bonds, dangling chains, or post-chain-rupture

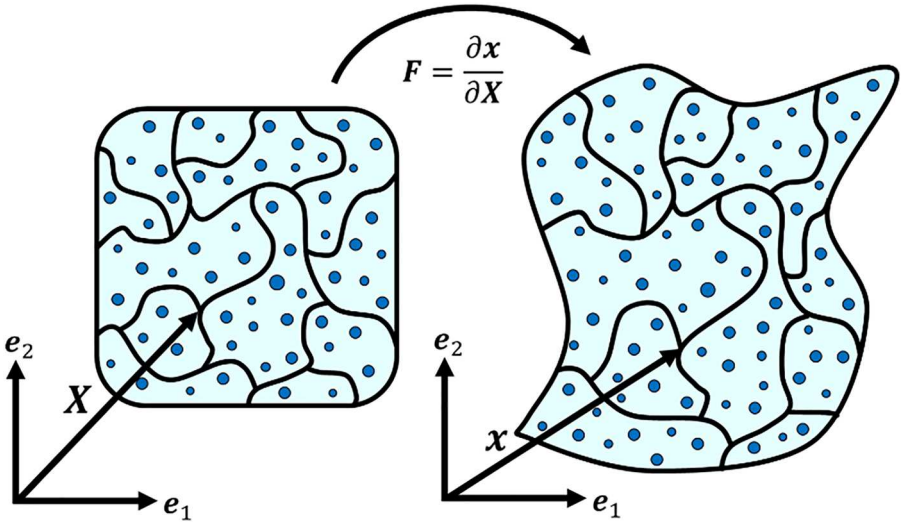

Fig. 2. Deformation of a gel: An arbitrary gel network is illustrated in its reference (left) and current (right) configurations after undergoing some compressible deformation $\boldsymbol{F}$. Polymer chains are depicted as black curves, while solvent is represented by the blue background and blue circles. The position of an arbitrary crosslink is illustrated in its reference ($\boldsymbol{X}$) and current ($\boldsymbol{x}$) positions with respect to the orthonormal basis.

landscapes. In reality, the local positions of dangling chains and the distribution of crosslinks in a gel are heavily dependent on local solute-solvent interactions and resulting osmotic pressure gradients (Daoud and Cotton, 1982; Flory and Rehner, 1943a, 1943b; Huissmann et al., 2009). Furthermore, existing mesoscopic approaches are limited in predicting the initial topologies of gels as a function of macromer functionality (governing the number of potential crosslinking interactions), as-prepared solution concentration (Akagi et al., 2010; Lange et al., 2011), molecular weight, or solvent quality. Yet these are the types of parameters which experimentalists may control during gel fabrication.

To address these limitations, we here adapt a recently developed mesoscale numerical framework (Wagner et al., 2021), to the case of PEG-based gels. The current work is novel two significant ways. Firstly, it considers the effects of osmotic pressure on global swelling of traction boundaries. While previous works enforced volumetric deformation through the empirically motivated displacement of network boundaries (Sugimura et al., 2013; Zhang et al., 2015), we here compute the degree of swelling based on the competition between global osmotic pressure (as predicted via Flory-Huggins theory) and the hydrostatic component of polymer network stress. Secondly, we introduce a scaling law to estimate the local polymer concentration as a function of the average mesh size, and spatial crosslink distribution. Previous works have employed more general methods of homogenization such as "explosion-contraction" Monte Carlo (MC) algorithms with Lennard-Jones potentials between nodes (Zhang et al., 2015). However, the distribution of polymer in a gel depends significantly on solute-solvent interactions (Daoud and Cotton, 1982; Huissmann et al., 2009; Johner and Lee, 2018; Jusufi et al., 1999; Lue and Kiselev, 2002). Therefore, we introduce a physically motivated method in which the spatial arrangement of macromers is governed by solute-concentration dependent gradients in osmotic pressure that introduce effective mixing forces. Thus, this model considers first-order physics that enable the *ab initio* simulation of gel networks, thereby requiring less *a priori* knowledge of gel microstructure over previous approaches and instead enabling predictive design of gels with certain topologies. To support *ab initio* predictive design, input parameters to this model correspond directly to typical control parameters during gel fabrication - namely, macromer molecular weight (M_w), solvent type (whose effects are coarsely captured through the Flory-Huggins mixing parameter, χ), normalized pre-gelation polymer concentration (ϕ^*), and macromer functionality (f) (Akagi et al., 2010; Lange et al., 2011; Matsunaga et al., 2009b, 2009a; Sukumar and Lopina, 2002).

The remainder of this work is structured as follows. In Section 2, we briefly overview the continuum mechanics approach commonly used to model global swelling mechanics of gels. This introduces readers to the significant concepts of osmotic pressure (governed by the free energy of mixing between polymer and solvent) and network stress (governed by strain energy of the polymer network). We then examine these features' counterparts at the network scale. In Section 3, we introduce the novel scaling law that relates local osmotic pressure gradients to microstructural crosslink distribution, and the single-chain force-extension relation that drives global network stress. We also describe the numerical implementation of not only these features, but also the macro-scale theory discussed in Section 2. In Section 4, we demonstrate that this model accurately predicts topological and mechanical characteristics of sol-gels (i.e., polymer suspensions turned to gels) during mixing, gelation, equilibrium swelling, and elastic deformations under plane stress boundary conditions. Finally, Section 5 concludes by exploring the effects of network topology on damage onset in permanent gels.

2. Flory-Rehner theory for global equilibrium of gels

Polymeric gels are comprised of networks of high molecular weight chains crosslinked to one another. When these networks are

submersed into a low molecular weight solvent there is an entropic increase associated with the interstitial penetration of liquid into the polymeric network. Additionally, in cases where there is energetic favorability between solvent-polymer interactions (as opposed to interpolymer or solvent-solvent interactions), there is also an enthalpic contribution to mixing. Together, these contributions lead to some effective osmotic pressure that induces transport of solvent into the network, inducing swelling. In this work, we consider the effects of osmotic pressure on not only the global mechanics (i.e., equilibrium swelling and traction boundary positions), but also local topology (i.e., the spatial distribution of crosslinks). In this section, we briefly outline the Flory-Rehner continuum mechanics theory used to predict the global swelling mechanics of gels (Flory and Rehner, 1943b).

The Flory-Rehner approach treats gels as a two-state solution in which the polymer network represents solute, while the interstitial fluid that causes swelling represents solvent (Fig. 2). Through this approach the Helmholtz free energy of the mixture is taken as the sum of the elastic strain energy (ψ_{el}) stored in the polymeric chains, and the free energy of mixing (ψ_{mix}) between solute and solvent as:

$$\psi = \psi_{el}(\boldsymbol{F}) + \psi_{mix}(\phi) \tag{1}$$

Here, $\boldsymbol{F} = \partial \boldsymbol{x}/\partial \boldsymbol{X}$ is the elastic deformation gradient (where $\boldsymbol{X}$ and $\boldsymbol{x}$ represent the reference and current crosslink positions of the network, respectively, as depicted in Fig. 2), and $\phi = V_p/V$ is the volume fraction of polymer (where V_p is the total volume of the polymer in the network and V is the total volume enveloped by the gel).

At mechanical equilibrium in the absence of body forces, the Cauchy stress state ($\boldsymbol{\sigma}$) of the gel must obey the differential equation:

$$\nabla \cdot \boldsymbol{\sigma} = \boldsymbol{0} \tag{2}$$

where ∇ is the differential operator in the current configuration, and $\boldsymbol{\sigma} = \boldsymbol{\sigma}_{el} + \boldsymbol{\sigma}_{mix}$ may be decomposed into its elastic network ($\boldsymbol{\sigma}_{el}$) and mixing ($\boldsymbol{\sigma}_{mix}$) components. It can be shown that the forms of these stresses arise from the minimization of the free energy and may therefore be directly derived from Eq. (1). The Cauchy stress is thus expressed as:

$$\boldsymbol{\sigma}_{el} = 2J^{-1}\boldsymbol{B} \cdot \frac{\partial \psi_{el}}{\partial \boldsymbol{B}} \tag{3}$$

where $\boldsymbol{B} = \boldsymbol{F}\boldsymbol{F}^{\mathbf{T}}$ is the left Cauchy-Green or finger deformation tensor, and $J = \det(\boldsymbol{F})$ denotes the relative change of volume of the gel (i.e., $J = V/V_0$ given a reference volume of V_0). The mixing stress emerges as an isotropic pressure (i.e., osmotic pressure) of the form:

$$\boldsymbol{\sigma}_{mix} = \pi \boldsymbol{I} \tag{4}$$

To compute π we consider that the solute consists of long chains of N bonded mers or Kuhn segments. The mixing entropy of a Kuhn segment may be written as $N^{-1}\phi \ln\phi$ and ψ_{mix} is given by (Doi, 2013):

$$\psi_{mix} = \frac{k_b T}{v}\left[\frac{\phi}{N}\ln\phi + (1-\phi)\ln(1-\phi) + \chi\phi(1-\phi)\right] \tag{5}$$

where k_b is the Boltzmann constant, T is the ambient temperature, v is the volume of a Kuhn segment, and χ is the Flory-Huggins solubility parameter ($\chi = 0.5$ for theta solvent in which polymers behave ideally as freely jointed chains, and $\chi \leq 0.5$ indicates that mixing will occur). Through Eq. (5), we may compute the amount of mixing work needed to expand or contract the gel by some incremental amount dV as:

$$\pi dV = -d(V\psi_{mix}) \tag{6}$$

where osmotic pressure, π, constitutes the pressure needed to maintain a given volume. Differentiating the right-hand side of Eq. (6) with respect to V gives π as:

$$\pi = \frac{k_b T}{v}\left[\frac{\phi}{N} - \ln(1-\phi) - \phi - \chi\phi^2\right] \tag{7}$$

For detailed derivations of Eqs. (5)–(7), readers are encouraged to read *Soft Matter Physics* by Doi (2013). From Eq. (7), we see that osmotic pressure is zero when $\phi = 0$, and pressure increases monotonically with respect to ϕ for good solvent in which mixing is favored ($\chi \leq 0.5$). This drives solvent from regions of lower-to-higher solute concentration.

Eq. (7) will prove useful in tracking the local osmotic pressure of the network model as described in Section 3.1. However, to consider the effects of osmotic pressure on global swelling, let us instead express Eq. (7) in terms of the volumetric change, J, of the overall gel as measured with respect to its dry state. Assuming the amount of polymer in the gel is conserved and that all volumetric change is driven by flux of solvent, then $J = \phi_0/\phi$ where ϕ_0 is the polymer volume fraction of the dry network. Substituting this into Eq. (7) gives:

$$\pi = \frac{k_b T}{v}\left[\frac{1}{JN} - \ln\left(1 - \frac{1}{J}\right) - \frac{1}{J} - \frac{\chi}{J^2}\right] \tag{8}$$

Note that the first term in Eq. (8) drops out with the assumption that $N \to \infty$, as appropriate for the case of gels containing large polymer networks. Eqs. (2), (3), and (8) collectively define the global equilibrium condition of a gel. While Flory-Rehner theory provides the governing equilibrium equations for a gel at the macro-scale, it neglects any local evolutions of spatial crosslink distribution. In the following sections we demonstrate how the concepts of local osmotic pressure gradients and single-chain elastic strain

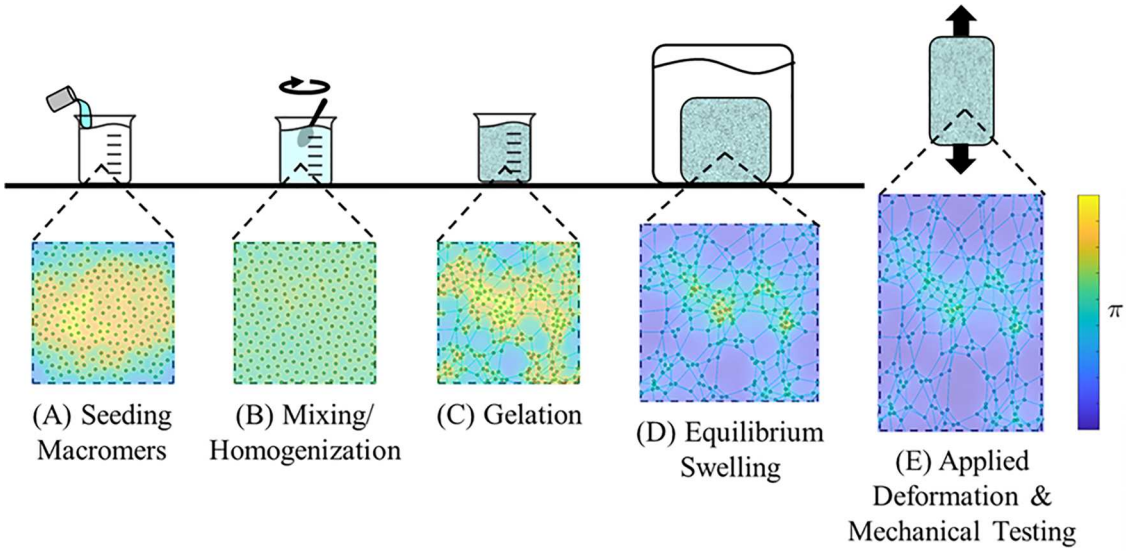

Fig. 3. Chronological steps of numerical model: (A) An RVE is seeded with macromers (or "nodes") whose centers are depicted as circles. (B) The macromers are positionally equilibrated by effective osmotic mixing forces. (C) The macromers are bonded to form a gelated network. (D) The network expands, decreasing the osmotic pressure, until the condition of Eq. (2) is met. (E) Deformation is applied to the boundaries of the RVE. The heat map represents normalized, local osmotic pressure. Dangling chains are not explicitly modeled and are therefore not shown in figures throughout this work.

energy may be leveraged to update topology in the discrete network model.

3. The network model

The numerical framework adopted here was introduced by Wagner et al. (2021). The chronological stages modeled by this framework are meant to mimic the *ab initio* processes of gel fabrication and mechanical experimentation as illustrated in Fig. 3. First, representative volume elements (RVEs) are initiated as square domains with periodic boundary conditions, centered at the Cartesian origin. The sizes of RVEs were set based on the convergence of stress response for increasingly large domains (see Appendix A). Star-shaped macromers or "nodes" are then seeded at coordinates $\boldsymbol{x}^{\alpha}$ using a Poisson's point process where the index α denotes the node number ($\alpha \in [1, \mathcal{N}]$) (Fig. 3A). Once initially seeded, the positions of nodes are equilibrated as governed by osmotic mixing forces (Fig. 3B). Nodes may remain unattached to model polymer suspensions, or their chains may be telechelically bonded to one another to mimic gelation (Fig. 3C). The RVEs are then prescribed some combination of traction and displacement boundaries to mimic experimental conditions such as equilibrium swelling (Fig. 3D) and applied deformations (Fig. 3E). In this section, we detail the effective mixing forces that act on macromers in star-shaped polymer suspensions or crosslinks in gel networks. We then review the chain attachment algorithm used to mimic gelation and describe the entropic chain forces that act on nodes in the crosslinked networks. Next, we describe how nodes' positions are iteratively equilibrated and network stress is computed at each discrete deformation or network reconfiguration step. Finally, we overview the various boundary conditions used over the course of this work and list the input parameters associated with the network model.

3.1. Local effects of osmotic pressure

We begin by examining the local effective mixing forces, as these are relevant for both the initial polymer suspensions and post-gelation networks. In this subsection we introduce the novel scaling law used to estimate spatial solute concentration gradients, which in turn govern effective pressure-gradient mixing forces. We then detail the numerical methods used to compute said forces.

3.1.1. Local scaling of solute concentration and effective mixing forces

In many polymeric materials such as dry elastomers (Bergström and Boyce, 2001; Flory, 1985) volume exclusion (i.e., repulsive contact potentials) will dominate the effective macromer or crosslink distributions. However, in this work and in the broader context of gels, polymer packing fractions are generally on the order of 0.01–0.1, such that the separation distances between macromers or crosslinks are significantly larger than the size of a mer ($\sim b$) or length scale of volume exclusion interactions. As such, network topology of gels or radial distribution of polymer in suspensions (Huissmann et al., 2009; Krakoviack et al., 2003) is instead governed by the effective mixing forces ($\boldsymbol{f}^{\pi}$) introduced by gradients in osmotic pressure (Horkay and Lin, 2009). Osmotic pressure, as described by Eq. (7), depends on both the local solute concentration (through ϕ) and favorability of solute-solvent interactions (characterized by χ). At the mesoscale, ϕ evolves locally as a function of the positions, $\boldsymbol{x}^{\alpha}$, of macromers or crosslinks (i.e., "nodes"). While scaling laws such

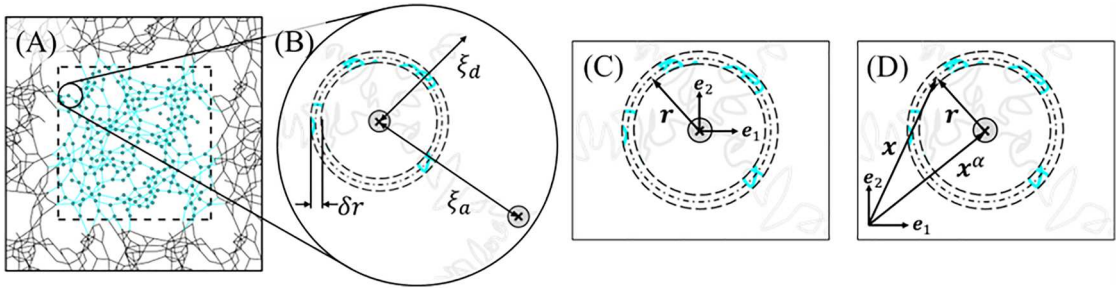

Fig. 4. Solute concentration scaling in a gel: (A) An RVE containing an arbitrary network is displayed. (B) A close-up schematic of an arbitrary crosslink from (A) is shown. A differential ring of width δr is enclosed by dashed lines. A dangling chain is depicted and posited to have an approximate end-to-end length of $\xi_d \approx \sqrt{N}b$. An attached chain is also depicted and posited to have an approximate end-to-end length, ξ_a, that is the same as the network's average attached chain length. (C) A differential ring at radial distance $|\boldsymbol{r}|$ with respect to the local reference frame (i.e., crosslink position) is displayed. (D) The same differential ring from (C) is displayed, with the material point $\boldsymbol{x} = \boldsymbol{x}^\alpha + \boldsymbol{r}$ denoted in the global reference frame. (B–D) The segments of polymer chain residing within the differential ring are shaded cyan.

as that introduced by Daoud and Cotton (1982) or Birshtein and Zhulina (1990, 1984) have been developed to predict the concentration gradient surrounding star-shaped polymers in solvent of varying quality, discrete numerical investigation of these relationships has called their ability to predict local swelling into question (Hsu et al., 2004). A great deal of research has been conducted through Monte Carlo and molecular dynamics simulations on the effective interactions between star shaped polymers, as well (Hsu et al., 2004; Huissmann et al., 2009; Johner and Lee, 2018; Jusufi et al., 1999; Krakoviack et al., 2003; Lue and Kiselev, 2002). These include the study of both dilute and concentrated systems. Nevertheless, few (if any) such studies have been conducted in the context of percolated gels comprised of star-shaped polymers, despite the fact that tetra-PEG macromers in solution have verifiably different concentration gradients than those in a percolated network (Matsunaga et al., 2009b, 2009a). Indeed most of the literature on the structure of such gels is empirically-gotten (Akagi et al., 2010; Matsunaga et al., 2009b; Schwenke et al., 2011; Shibayama et al., 2019; Sukumar and Lopina, 2002), and appropriate scaling laws for solute concentration gradients are, to our knowledge, not available in existing works. Therefore, for our purposes, we begin by introducing a simple scaling law for solute concentration, specific to the case of star-shaped crosslinkers in the low functionality regime (here, $f \in [3, 10]$).

Consider an arbitrary, 2D network such as that depicted in Fig. 4A, which has an average nearest crosslink-to-crosslink separation or "mesh size" $\bar{\xi}$, and in which each crosslink has a functionality of f; each arm has N Kuhn segments; and each Kuhn segment has a length of b and width of w. Let us first examine the solute concentration function due to a single node at position, $\boldsymbol{x}^\alpha$, as we move radially outwards from its center to some position $\boldsymbol{r}$. Here we temporarily treat $\boldsymbol{x}^\alpha$ as our reference position and we denote the solute concentration function due to this isolated node as $\varphi^\alpha(\boldsymbol{r})$. To estimate $\varphi^\alpha(\boldsymbol{r})$, we envision an infinitesimal ring of width δr, at distance $r = |\boldsymbol{r}|$ from $\boldsymbol{x}^\alpha$, as illustrated in Fig. 4B,C. In 2D, the local polymer packing fraction within this ring is defined as the area of polymer residing within it (δA) divided by the total ring area ($2\pi r \delta r$):

$$\varphi^\alpha(\boldsymbol{r}) = \frac{\delta A}{2\pi|\boldsymbol{r}|\delta r} \tag{9}$$

The area of polymer inside the ring may be written as:

$$\delta A = (fbw)\delta N \tag{10}$$

where bw represents the area of a single mer and δN represents the number of mers inside the ring belonging to a single chain (so that $f\delta N$ represents the contribution from all chains). For simplicity, we posit that a polymer chain remains evenly coiled and distributed in the space between the crosslinks it spans (Fig. 4B). We also coarsely impose that it is equiprobable to find polymer at any azimuthal position around the crosslink (i.e., radial symmetry). Under these conditions, δN scales proportionately with the number of Kuhn segments per chain (N), and the ring thickness (δr), and is inversely related to the average mesh size ($\bar{\xi}$):

$$\delta N \sim N\bar{\xi}^{-1}\delta r \tag{11}$$

This notion assumes that at low functionality, steric interactions between adjacent chains are minimal so that the chains may coil freely. Combining Eqs. (9)–(11) gives the estimated solute area at distance r in 2D as:

$$\delta A \sim fNbw\bar{\xi}^{-1}\delta r \tag{12}$$

Substituting Eq. (12) into Eq. (9) provides that the local solute fraction scales with $|\boldsymbol{r}|$ according to:

$$\varphi^\alpha(\boldsymbol{r}) \sim \begin{cases} 1, & |\boldsymbol{r}| < \dfrac{fNbw}{2\pi}\bar{\xi}^{-1} \\ \dfrac{fNbw}{2\pi|\boldsymbol{r}|}\bar{\xi}^{-1}, & \dfrac{fNbw}{2\pi}\bar{\xi}^{-1} < |\boldsymbol{r}| \end{cases} \tag{13}$$

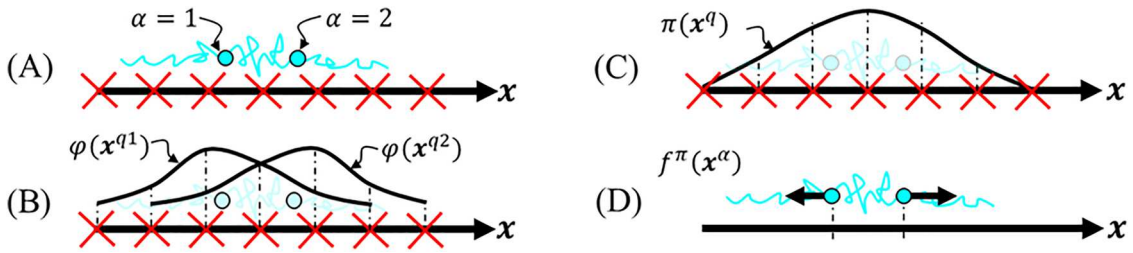

Fig. 5. Numerical implementation of effective mixing forces in 1D: (A) A two-node ($\alpha \in [1,2]$) system is displayed in 1D along spatial dimension x. The nodes are depicted as blue circles with blue chains connecting them, and the underlying Eulerian grid is depicted as red exes. (B) The local solute concentration function due each node, $\varphi(\boldsymbol{x}^{q\alpha})$, is estimated using Eq. (15) and illustrated at the positions of the Eulerian query points, $\boldsymbol{x}^q$. (C) The combined local solute concentration function, $\phi(\boldsymbol{x}^q) = \sum_{\alpha=1}^{2} \varphi(\boldsymbol{x}^{\alpha q})$ is computed and then used to calculate $\pi(\boldsymbol{x}^q)$ through Eq. (7), which is displayed at the positions $\boldsymbol{x}^q$. (D) The effective mixing forces, $\boldsymbol{f}^\pi(\boldsymbol{x}^q)$, are computed through Eqs. (17) and (18) and then interpolated at the positions of the nodes to get $\boldsymbol{f}^\pi(\boldsymbol{x}^\alpha)$, which is illustrated as black vectors at positions $\boldsymbol{x}^\alpha$. The sizes of the arrows indicate the relative magnitudes of effective forces. (B,C) The functions $\varphi(\boldsymbol{x}^{q\alpha})$ and $\pi(\boldsymbol{x}^q)$ are smoothly interpolated between query points for illustrative purposes, although actual interpolation takes place between (C) and (D).

with the added condition that $\varphi^\alpha(\boldsymbol{r})$ cannot exceed unity. To compute $\bar{\xi}$, we consider that many of the chains are fully attached to the network so that their end-to-end separation is governed by the average mesh size of the system. Meanwhile, the average length of dangling chains depends instead on their tethered diffusion in the solvent. Taking c and $1-c$ as the relative fractions of attached and dangling chains, respectively, then we may estimate the mean mesh size as the sum of weighted contributions from each population:

$$\bar{\xi} \approx c\bar{\xi}_a + (1-c)\bar{\xi}_d \tag{14}$$

where $\bar{\xi}_a$ and $\bar{\xi}_d$ are the average measured end-to-end distance of an attached and dangling chain, respectively (Fig. 4B). While the average end-to-end length of attached chains, $\bar{\xi}_a$, may be measured explicitly, we impose that dangling chains behave ideally (since we are primarily concerned with gels in good solvent) and therefore have a mean end-to-end length of $\bar{\xi}_d = \sqrt{N}b$.

Eq. (13) provides $\varphi^\alpha(\boldsymbol{r})$ as a function of radial distance with respect to the reference position $\boldsymbol{x}^\alpha$ (Fig. 4C). However, with respect to the global reference frame, we instead write:

$$\varphi^\alpha(\boldsymbol{x}) \sim \begin{cases} 1, & |\boldsymbol{x}-\boldsymbol{x}^\alpha| < \dfrac{fNbw}{2\pi}\bar{\xi}^{-1} \\ \dfrac{fNbw}{2\pi|\boldsymbol{x}-\boldsymbol{x}^\alpha|}\bar{\xi}^{-1}, & \dfrac{fNbw}{2\pi}\bar{\xi}^{-1} < |\boldsymbol{x}-\boldsymbol{x}^\alpha| \end{cases} \tag{15}$$

where $\boldsymbol{x} = \boldsymbol{x}^\alpha + \boldsymbol{r}$ (Fig. 4D). In a system of $\mathcal{N}$ macromers, the overall solute concentration function may then be taken as the sum of $\varphi^\alpha(\boldsymbol{x})$ for $\alpha \in [1,\mathcal{N}]$ as:

$$\phi(\boldsymbol{x}) = \Phi^{-1} \sum_{\alpha=1}^{\mathcal{N}} \varphi^\alpha(\boldsymbol{x}) \tag{16}$$

where $\Phi = \int_V \phi(\boldsymbol{x}) dV/(VJ\phi_0)$ is a normalization scalar that enforces conservation of mass (i.e., that the average value of $\phi(\boldsymbol{x})$ equals the globally computed solute fraction, $J\phi_0$).

Given $\phi(\boldsymbol{x})$ the spatial osmotic pressure function, $\pi(\boldsymbol{x})$, may be computed directly using Eq. (7). To compute the effective force, $\boldsymbol{f}^\pi(\boldsymbol{x})$, imposed by local gradients in $\pi(\boldsymbol{x})$, we invoke that the amount of work, $\boldsymbol{f}\cdot d\boldsymbol{x}$, needed to move a solute particle by a displacement of $d\boldsymbol{x}$ must be equal and opposite to the consequential change in the local free energy of mixing, $-Vd\pi$ (Doi, 2013; Salari et al., 2013). Thus, we may write the pressure gradient force relation as:

$$\boldsymbol{f}^\pi \cdot d\boldsymbol{x} = -Vd\pi \tag{17}$$

where V is the approximate volume of solvent displaced by the movement of a macromer ($V \approx fNbw^2$). Solving Eq. (16) for $\boldsymbol{f}^\pi$ gives the local driving force of solute due to mixing as:

$$f^\pi(\boldsymbol{x}) = -\frac{N}{2} fbw^2 \nabla\pi(\boldsymbol{x}) \tag{18}$$

where $\nabla\pi$ denotes $d\pi/d\boldsymbol{x}$, or the spatial pressure gradient in the current configuration. Although the scaling relation of Eq. (15) is presented for 2D networks, an analogous relation may be derived to apply this method to 3D networks. Eqs. (16) and (18) remain applicable, regardless of dimensionality (i.e., whether spatial vectors are one, two, or three dimensional).

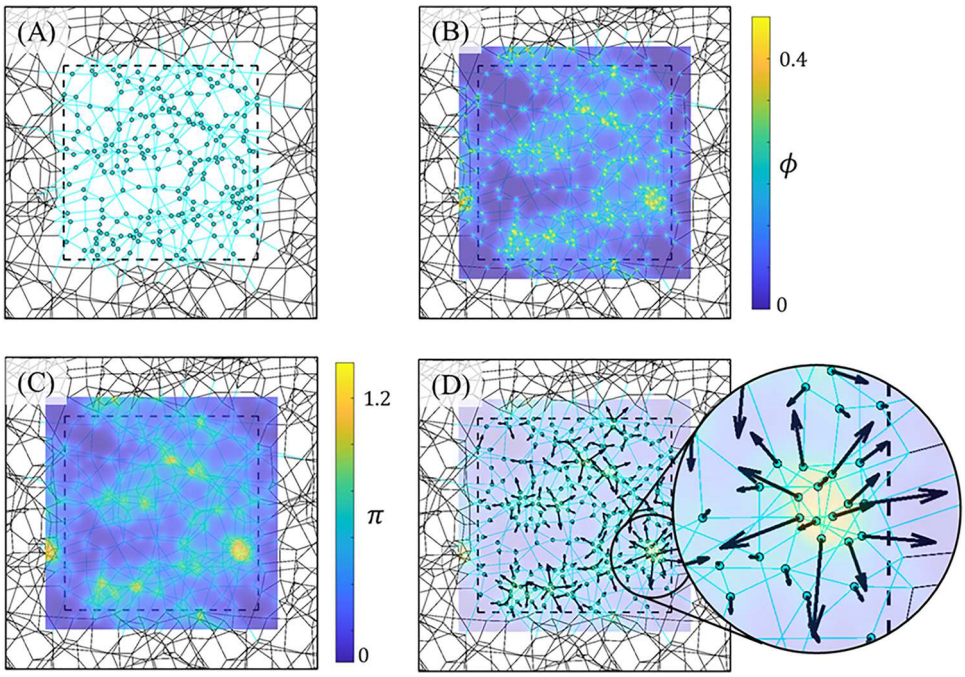

Fig. 6. Outcomes of numerical implementation in 2D: (A) An equilibrated numerical gel network is displayed. (B) The estimated polymer packing fraction function ($\phi(\boldsymbol{x}^q)$) is displayed at the query points ($\boldsymbol{x}^q$) of the Eulerian grid. (C) The corresponding local osmotic pressure function ($\pi(\boldsymbol{x}^q)$) is displayed. (D) The pressure gradient force ($\boldsymbol{f}^{\pi}(\boldsymbol{x}^{\alpha})$) is computed and interpolated at the positions of crosslinks (black arrows). The heat map of $\pi(\boldsymbol{x}^q)$ from (C) remains faintly displayed in (D) to visually illustrate how forces follow the local osmotic pressure gradient. A close-up of osmotic pressure forces around a cluster of nodes is also depicted for clarity. (B–D) The heat maps of $\phi(\boldsymbol{x}^q)$ and $\pi(\boldsymbol{x}^q)$ are interpolated between query positions for illustrative purposes.

3.1.2. . Numerical implementation of mixing force

As discussed in the previous section, osmotic mixing forces depend on local gradients in osmotic pressure, which in turn depend on the local solute concentration, $\phi(\boldsymbol{x})$. To approximate a differentiable landscape of osmotic pressure within the numerical framework, $\phi(\boldsymbol{x})$ is computed on a discretized, Eulerian grid, whose node positions are defined by the vector set $\boldsymbol{x}^q$. This Eulerian grid and the numerical methods described in this subsection are illustrated schematically through Fig. 5 for a simple 1D, two-node system. The solute packing fraction at each q^{th} query point on the Eulerian grid as a function of its distance from each a^{th} node in the domain, $\varphi(\boldsymbol{x}^{q\alpha})$, is calculated using Eq. (15) (Fig. 5A,B). Note that here, $\boldsymbol{x}^{\alpha q} = |\boldsymbol{x}^q - \boldsymbol{x}^{\alpha}|$ is the distance between node α and query point q , and is synonymous with $|\boldsymbol{x} - \boldsymbol{x}^{\alpha}|$ in continuous space from Eq. (15). The solute concentration functions due to each crosslink, $\varphi(\boldsymbol{x}^{\alpha q})$, are then summed over all nodes per Eq. (16) to get the overall solute concentration function on the Eulerian grid, $\phi(\boldsymbol{x}^q) = \Phi^{-1}\sum_{\alpha=1}^{\mathcal{N}}\varphi(\boldsymbol{x}^{\alpha q})$. To compute Φ in the numerical framework, the overall solute concentration is taken as $\phi_0 J = A_p/A_{RVE}$, where $A_p = \mathcal{N}fNbw$ is the total solute area in the RVE and A_{RVE} is the total RVE area. The solute concentration function, $\phi(\boldsymbol{x}^q)$, is then used to compute the osmotic pressure function $\pi(\boldsymbol{x}^q)$ on the Eulerian grid through Eq. (7) (Fig. 5C). Given $\pi(\boldsymbol{x}^q)$, the spatial gradient in pressure is linearly interpolated at position $\boldsymbol{x}^q$ using a central difference approximation:

$$\nabla\pi(\boldsymbol{x}^q) \approx \frac{\pi(\boldsymbol{x}^{q+1}) - \pi(\boldsymbol{x}^{q-1})}{2\Delta x} \tag{19}$$

where $\Delta x \sim \bar{\xi} \times 10^{-1}$ is the grid spacing, which is set less than an order of magnitude smaller than the network's mesh size to approximate smooth crosslink motion. Finally, $\nabla\pi(\boldsymbol{x}^q)$ is substituted into Eq. (18) to compute the effective mixing force function, $\boldsymbol{f}^{\pi}(\boldsymbol{x}^q)$, which is then linearly interpolated at the positions of the crosslinks in the network (Fig. 5E).

Fig. 6 illustrates the outcome of this numerical implementation via snapshots of the network model. Fig. 6A, C and D are 2D analogues to the 1D schematics of Fig. 5A, C and D, respectively. Again, while the framework adapted here is 2D, this method could also be incorporated into 3D frameworks. Fig. 6D displays a close-up view of the effective mixing forces at the crosslink positions, $\boldsymbol{f}^{\pi}(\boldsymbol{x}^{\alpha})$, around a higher density cluster, thus demonstrating how this method drives crosslinks away from regions of higher solute concentration for good solvent (here $\chi = 0.5$), thus fulfilling the role of an effective pairwise repulsion between neighboring crosslinks. Significantly, $\boldsymbol{f}^{\pi}(\boldsymbol{x})$ induces homogenization of simulated macromers in good solvent ($\chi \leq 0.5$) prior to gelation. In homogenizing the solution before nodes are attached to one another, mixing forces mitigate any boundary effects introduced by the way in which nodes are seeded into the periodic RVE. In effect, through $\boldsymbol{f}^{\pi}(\boldsymbol{x}^{\alpha})$, the model mimics the mixed conditions of solutions prior to crosslinker polymerization

3.2. . Gelation and entropic chain forces

Once macromers are seeded and initial homogenization due to effective mixing forces is completed, the system may be gelated without biased formation of defects near the RVE's boundaries. This is achieved using the Rouse diffusion-based chain attachment introduced by Wagner et al. (2021). Within a given timestep, the probability of attachment between two chains belonging to neighboring nodes is defined according to the Poisson's process:

$$dP_a = k_a e^{-k_a t} dt \tag{20}$$

where k_a is the rate of attachment. Given that the chains are tethered to their permanent crosslinks, we define k_a according to a scaling law based on Rouse diffusion to define k_a as (Wagner et al., 2021):

$$k_a = \frac{1}{\tau_0}\left(\frac{b}{d}\right)^4 \tag{21}$$

where d is the distance between neighboring nodes and τ_0 is the time it takes a chain's tip to diffuse the length of one of a Kuhn segment, b. For simplicity, nodes are not allowed to attach to themselves. However, nodes may attach to each other more than once to capture the double, triple and quadruple-link defects observed by Lange et al. (2011) and Schwenke et al. (2011) and discussed in Section 4.2. Attachment events are checked iteratively until the network achieves greater than 95% connectivity.

Note that the introduction of bonded chains mandates computation of single-chain forces derived from the entropic penalty of polymer extension. The strain energy function of entropic chains is suitably modeled using the Padé approximation (Cohen, 1991) of Langevin chains given by (Wagner et al., 2021):

$$\psi_c = k_b T\left[\frac{\lambda^2}{2} - N\log\left(N-\lambda^2\right)\right] \tag{22}$$

where λ is the chain stretch given by $\lambda = r/\sqrt{N}b$ and r is the chain's end-to-end length. This yields a force-stretch relation of the form:

$$f = \frac{3k_b T}{\sqrt{N}b}\lambda\left(\frac{\lambda^2-3N}{\lambda^2-N}\right) \tag{23}$$

As in the case of polymers (Kienberger et al., 2000) the force in this model diverges for chains extended near their full contour lengths (or $\lambda \to \sqrt{N}$), thus also capturing the enthalpic effects of bond stretching (Oesterhelt et al., 1999).* Chain forces always act in tension and remain aligned with their chains' end-to-end vectors, $\boldsymbol{r}$.

3.3. . Force equilibration and stress formulation

Since macromers or crosslinks are seeded stochastically, they do not begin at equilibrium. Additionally, processes such as bond attachments, equilibrium swelling, applied deformation, and bond rupture also drive the crosslinks out of equilibrium. However, equilibrium is assumed throughout this work based on the assumptions that solvent may move freely into or out of the networks as needed to maintain thermodynamic equilibrium, and any loading rates are applied significantly slower than the rate of solvent transport. Therefore, nodes are iteratively equilibrated to their lowest energy state at every network reconfiguration or deformation step (i.e., "timestep"). This is done using the overdamped method detailed in Wagner et al. (2021), which updates the positions of the nodes from iteration k to $k+1$ according to:

$$\boldsymbol{x}_{k+1}^{\alpha} = \boldsymbol{x}_k^{\alpha} + \nu^{-1}\boldsymbol{f}_k^{\alpha} \tag{24}$$

Here, ν is a numerical overdamping coefficient and $\boldsymbol{f}^{\alpha}$ is the net force acting on node α given by:

$$\boldsymbol{f}^{\alpha} = \sum_{\beta}\boldsymbol{f}^{\alpha\beta} + \boldsymbol{f}^{\pi} \tag{25}$$

where $\sum_{\beta}\boldsymbol{f}^{\alpha\beta}$ is the sum of node α's pairwise interaction forces with its neighboring nodes, β, and $\boldsymbol{f}^{\pi}$ is the osmotic pressure-dependent force of mixing detailed in Section 3.1. Since osmotic pressure-dependent forces, $\boldsymbol{f}^{\pi}$, depend on the local solute concentration, $\phi(\boldsymbol{x}^{\alpha})$ and osmotic pressure, $\pi(\boldsymbol{x}^{\alpha})$ these scalar fields are also iteratively updated throughout equilibration. Pairwise interaction forces, $\boldsymbol{f}^{\alpha\beta}$, consists of the tensile forces carried by attached polymer chains described in Section 3.2. For simplicity, monomer interactions between crossing chains (e.g., volume exclusion, entanglement, etc.) are here omitted and do not affect the forces of Eq. (25). Again, this is because effective osmotic pressure forces (as opposed to short-range monomer interactions) are taken as the first-order phenomenon affecting polymer distribution in gels (Daoud and Cotton, 1982). This treatment is justified by the relatively ideal network structure and minimized entanglement in low polydispersity (i.e., low molecular weight variance) PEG-based gels (Matsunaga et al., 2009b;

* Where indicated, Gaussian (i.e., ideal or linear) chains are used in lieu of Langevin chains. The force-extension of a Gaussian chain is given by $f = 3k_bT\lambda/(\sqrt{N}b)$ and does not diverge in the limit $\lambda \to \sqrt{N}$.

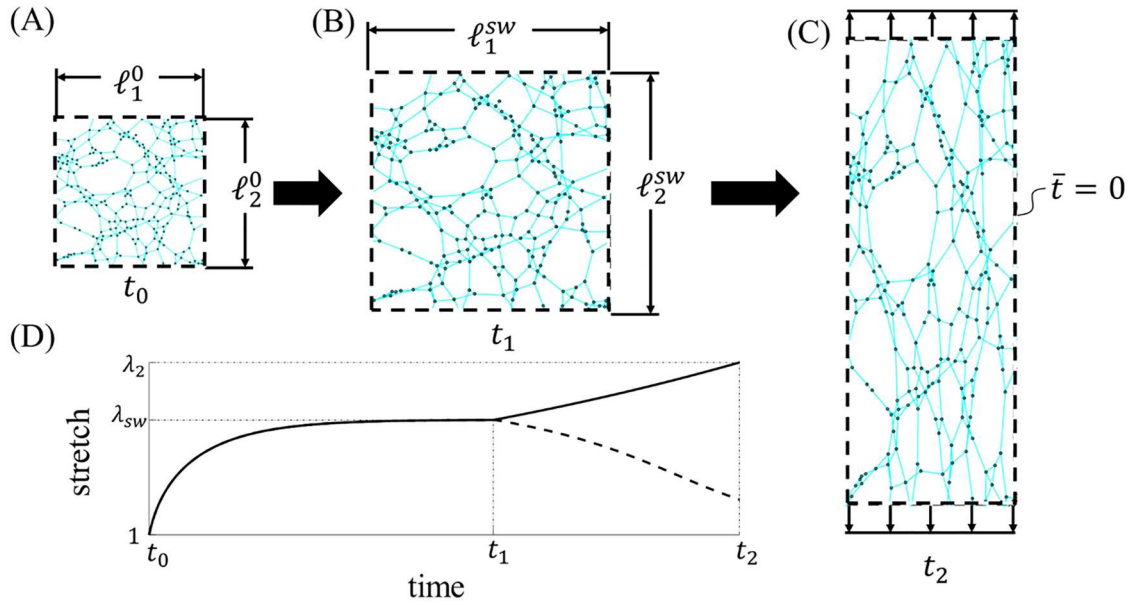

Fig. 7. Applied boundary conditions. (A,B) Stage I: A sample numerical gel network, which begins at (A) time t_0 with the dry, square dimensions $\ell_1^0 = \ell_2^0$, is depicted undergoing initial, unconstrained equilibrium swelling. (B,C) Stage II: From the (B) swollen state at time t_1, the network is then (C) stretched in the vertical direction at a constant strain rate of L_{22}. During this applied deformation, the RVE width is governed by the balance between σ_{11} and π. (D) A sample loading history (λ with respect to time) is depicted with t_0, t_1 and t_2 corresponding to the times of (A), (B), and (C), respectively. Dotted lines denote periodic boundaries.

Sugimura et al., 2013); the dilution of swollen gels in good solvent (which reduces the frequency of short-range monomer interactions); and the finding that the effects of intra-chain monomer volume exclusion diminish for longer polymer chains (Flory and Fisk, 1966).

Eqs. (24) and (25) are iterated until the mean and maximum unbalanced forces on the nodes move below 0.05 pN and 0.1 pN, respectively. These residual thresholds constitute roughly 0.2 and 0.4% of the force carried by a linear chain stretched to its full contour length, and thus sufficiently approximate the minimum energy state for the purposes of this work. Once equilibration is completed after each timestep, the entropic chain forces, $\boldsymbol{f}^{\alpha\beta}$, may be used to compute the instantaneous network stress through the virial formulation according to:

$$\boldsymbol{\sigma}_p = \frac{1}{2V} \sum_{\alpha}^{\mathcal{N}} \sum_{\beta} \boldsymbol{r}^{\alpha\beta} \otimes \boldsymbol{f}^{\alpha\beta} \tag{26}$$

where V is the RVE volume[†], and $\boldsymbol{r}^{\alpha\beta} = \boldsymbol{x}^{\alpha} - \boldsymbol{x}^{\beta}$ is the end-to-end vector between node α and its bonded neighbor, β (Wagner et al., 2021). Note that $\boldsymbol{\sigma}_p$ through Eq. (26) gives only the polymer network stress, which is counteracted by osmotic pressure π such that the overall material stress $\boldsymbol{\sigma}$ in the equilibrated swollen state is given by $\boldsymbol{\sigma}_p + \pi \boldsymbol{I} = \boldsymbol{0}$ when $\boldsymbol{F} = \boldsymbol{I}$.

3.4. . Equilibrium swelling and applied deformations

Once the networks are fully gelated, deformation is typically applied in two stages. First the gel network is permitted to swell isotropically and unconstrainedly from its initial arbitrary size to its equilibrated state (Fig. 7A). At this stage all four of the RVE's periodic edges are traction boundaries. In the second stage we apply mixed boundary conditions to the RVE to enforce a prescribed uniaxial tensile deformation of the gel (Fig. 7B). In both stages, stepping of the traction-free boundaries is conducted to satisfy the Flory-Rehner, global equilibrium condition from Eq. (2). While only the central RVE is depicted in images throughout this work, all RVEs are 2D periodic. Both displacement and traction boundaries are updated by stepping the position of the RVE edges, however the former are stepped to enforce some prescribed strain, while the latter are stepped to achieve some prescribed stress on the boundary.

During initial swelling, the dimensions of the RVE boundaries are updated iteratively according to:

$$\ell_1^{k+1} = \ell_1^k + \nu^{-1} \left[\ell_2^k \left(\pi - \sigma^h \right) \right] \tag{27}$$

[†] Since the RVE is 2D, its volume is taken as $V = \ell_1 \ell_2 \xi$ where ζ represents the thickness of the domain. Thickness is treated as a fitting parameter when comparing σ between 3D experimental results and the 2D model predictions.

Table 1
Primary model parameters.

Parameter	Value, Range	Units
Functionality, f	$[3, 10]$	NA
Molecular Weight, M_w	$[10, 200]$	kDa
Mixing Parameter, χ	0.5	NA
As-prepared Solute Fraction, ϕ^*	~ 2	NA

$$\ell_2^{k+1} = \ell_2^k + \nu^{-1}\left[\ell_1^k\left(\pi - \sigma^h\right)\right] \tag{28}$$

where ℓ_1^k and ℓ_2^k represent the length of the horizontal and vertical traction boundaries at iteration k, respectively, and ν is again some numerical overdamping coefficient. Eqs. (27) and (28) ensure that if the osmotic pressure exceeds the hydrostatic network stress ($\pi > \sigma^h$), then the domain increases in size and swelling continues. These equations are iterated until the residual difference between π and σ^h is below 0.004 kPa, which constitutes less than 1% of the overall hydrostatic network stress typically observed and provides ample convergence in the swollen equilibrium state.

Both Eqs. (27) and (28) are carried out during stage one of deformation (i.e., isotropic swelling). However, during the second stage of deformation, displacement of the vertical boundary is governed by the condition that:

$$\ell_2(t) = \ell_2^{sw}\exp(L_{22}t) \tag{29}$$

where ℓ_2^{sw} is the height of the RVE after isotropic equilibrium swelling is completed, L_{22} is the constant applied strain rate and t denotes time. During this stage, the Flory-Rehner condition (i.e., a traction-free condition) is maintained for the horizontal boundaries through the traction-free equilibrium condition that $\sigma_{11} + \pi = 0$. Therefore, the horizontal boundary is iteratively stepped via a displacement condition that is analogous to Eq. (28), given by:

$$\ell_1^{k+1} = \ell_1^k + \nu^{-1}\left[\ell_2^k(\pi - \sigma_{11})\right] \tag{30}$$

Again, the physicality of this boundary condition is contingent on the unhindered influx of solvent into the gel, as needed, and is therefore based on the assumption that the loading rate, L_{22}, is significantly smaller than the rate of solvent diffusion. After every step of boundary deformation during either stage, the network's crosslink positions are iteratively equilibrated using Eqs. (24) and (25).

3.5. Free parameters

Despite gels' complexity, this model requires the input of just four free parameters, as listed in Table 1. These parameters are the functionality (f), macromer molecular weight (M_w), solute-solvent interaction parameter (χ), and as-prepared solute concentration (ϕ^*). Solute concentration is taken as the solute volume fraction (ϕ) normalized by the overlap volume fraction (ϕ_{ol}) at which the star-shaped macromers' radii of gyration inter-penetrate one another. Note that the number of nodes is held constant across simulations such that ϕ^* is mediated by the initial size of the RVE during gelation. Both M_w and f are coupled with the chain length (L) of a single arm. Therefore, f and M_w are often paired, as indicated throughout the text, to fix L as f is swept.

For details on domain length scale and concentration calibration, see Appendix B. There are no relevant timescales included in this work since deformations are presumed to occur at a rate much slower than the diffusion rate of solvent and no rate-dependent bond detachments are included. However these timescales can and will be included in future works through the swelling kinetics theory of Tanaka and Fillmore (1979), force-dependent bond detachment rates (Bell, 1978; Eyring, 1935), and/or diffusion-dependent re-attachment rates (Stukalin et al., 2013; Wagner et al., 2021). Nonetheless, without any pertinent timescale, the deformation rate, L_{22}, is arbitrary and the more important consideration is how many steps in which the deformation is carried out. To achieve adequate sampling frequency, and properly isolate the effects of discrete bond rupture events, the deformation was applied in approximately 550 steps per simulation.

4. Gel topology and elastic response

The networks examined in this work are modeled after PEG-based gels for which there exists an abundance of experimental data, and which display exceptional spatial homogenization and high yield (> 90% chain connectivity) (Shibayama et al., 2019). Macromer functionality is specified throughout this section, but is most commonly set to $f = 4$ due to the large number of experimental studies on tetra-PEG[‡] gels (Akagi et al., 2010; Horkay et al., 2017; Matsunaga et al., 2009b; Shibayama et al., 2019; Wang et al., 2018). Unless specified otherwise, gels undergoing deformations are treated as if suspended in a solvent bath at thermodynamic equilibrium with the ambient environment. Additionally, all applied deformation rates are considered slower than the rate of solvent diffusion through the network such that rate-dependent solvent transport effects may be ignored. Together, these assumptions allow us to invoke that solvent

[‡] Gels constituting a specific molecular weight and functionality are referenced using the convention "<M_w> k <*Greek numerical prefix*>-PEG". For example, a gel comprised of 4-arm macromers with $M_w = 10$ kDa is referred to as a 10k tetra-PEG gel throughout the text.

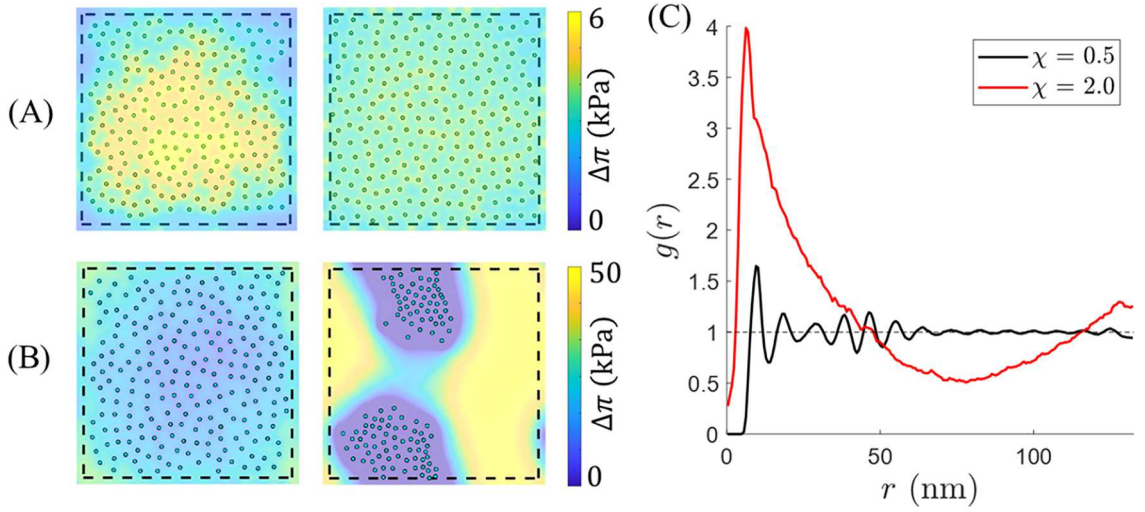

Fig. 8. Phase separation of polymer suspensions. (A,B) The evolution of macromer suspensions (10k tetra-PEG macromer) is displayed. The initial solutions (left) were forced into a relatively homogenous state using a Poisson's point process such that the more equilibrated systems (right) could evolve as governed solely by the local gradient in osmotic pressure. Evolutions are depicted for solvent qualities of (A) $\chi = 0.5$ (theta solvent), and (B) $\chi = 2$, resulting in full homogenization and phase separation, respectively. (C) The corresponding RDFs are displayed for both solvent qualities with χ as indicated in the legend.

moves into and out of the gel as needed to maintain equilibrium.

4.1. Homogenization and phase separation of polymer suspensions

Here we demonstrate the model's ability to predict homogenization or phase separation of polymer suspensions without the explicit inclusion of any repulsive or attractive pairwise potentials between nodes. A novelty of this approach is that it does not take homogenization of macromer's for granted before or after gelation, as in the case of other comparable approaches. Instead, the distribution of macromers is governed by the physics of solute-solvent interactions characterized by χ. Fig. 8A,B displays suspensions in which the centers of tetra-functional macromers are depicted. Two suspensions (for $\chi = 0.5$ and $\chi = 2$, respectively) are displayed as initiated (Fig. 8A,B, left) and after they have achieved the prescribed equilibrium criteria (Fig. 8A,B, right). To demonstrate that the local osmotic pressure, and not the initial macromer distribution is what causes phase separation, all networks are initiated with relatively high homogeneity using a pairwise Poisson's point process. Again, neither attractive nor repulsive pairwise potentials are included.

To characterize macromer distribution, we investigate the radial distribution function (RDF), $g(r)$, which quantifies the probability of finding two macromers at a given end-to-end distance. Peaks in $g(r)$ indicate correlation length scales (i.e., that there is a higher probability of finding two particles at a given pairwise separation distance). In contrast, values of $g(r)$ near or below unity indicates that particles are less correlated with one another and more correlated with empty space at a given length scale. When $\chi = 0.5$ (Fig. 8A) mixing and homogenization occur whereby the macromers evenly distribute and $g(r)$ appears periodic (Fig. 8C), indicating a degree of long-range order like that observed in concentrated colloidal and star-polymer suspensions (Mohanty et al., 2014; Padding and Briels, 2014) . Despite only accounting for solute-solvent interactions (as opposed to volume exclusion effects), such homogenization is consistent with the statistical mechanics predictions of Watzlawek et al. (1998), the MC studies of Hebbeker et al. (2018), or the higher fidelity MD results of Lee and Larson (2009) and Khoiroh et al. (2020) for suspensions in good solvent. However, when $\chi = 2.0$ this method predicts unstable phase separation that cannot be modeled using only volume exclusion interactions (Fig. 8B). Indeed, setting $\chi > 0.5$ effectively introduces depletion forces between solute particles. While it is tempting to phenomenologically introduce such forces via attractive regimes in effective pairwise potentials, it is well demonstrated that such forces vary locally with solute concentration (Bolhuis et al., 2001; Egorov, 2004; Jusufi et al., 1999; Krakoviack et al., 2003) and should therefore not be treated monolithically across a spatial domain. This method avoids such treatment and constitutes a more physically motivated method in which any effective depletion forces automatically evolve with local topological gradients.

While we have neglected the effects of volume exclusion interactions, Brownian diffusion, or entanglements between interpenetrating macromers, in the future these features could be easily combined with the methods introduced here. This would enable detailed studies of polymer suspensions in applications such as colloidal photonic crystals (Hosein et al., 2010; Riley and Watson, 2014). However, in the remainder of this work - unless specified otherwise - we focus on sol-gels in theta solvent ($\chi \approx 0.5$) based on experimental evidence that for tetra-PEG gels in the molecular weight range $M_w \in [5,40]$ kDa, the effective mixing parameter is within the tight range of $\chi \in [0.46, 0.49]$ (Matsunaga et al., 2009a). For such sol-gels, homogenization prior to gelation is reasonably assumed.

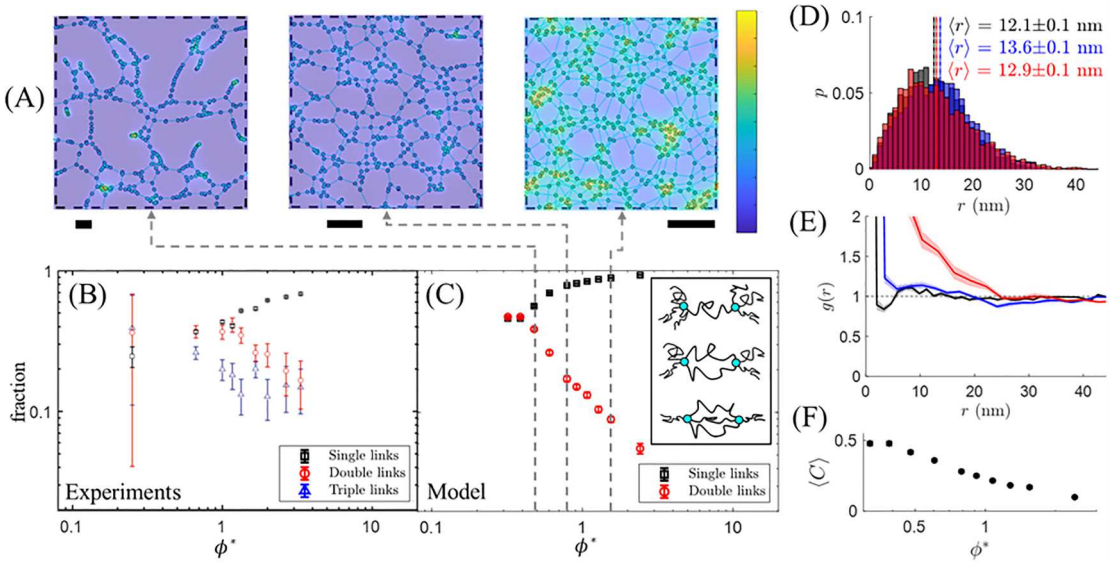

Fig. 9. Validation of the model's predicted *ab initio* topologies. (A) Sample networks gelated from low (left) to high (right) as-prepared concentration are depicted. The rightmost sample represents the network topology used for in silico experimentation throughout this work. All scale bars represent the contour length of a single chain (44 nm). The color bar indicates the local osmotic pressure, $\pi \in [0, 10]$ kPa. (B) The experimentally measured fractions of single links (black squares), double links (red circles), and triple links (blue triangles) are plotted with respect to the normalized as-prepared concentration depicted for a 10k tetra-PEG gel. Adapted with permission from Lange et al. (2011). Copyright 2011 American Chemical Society. (C) The fraction of single links (black squares) and double links (red circles) is plotted with respect to the normalized as-prepared concentration for the ensemble average of ten simulated 10k tetra-PEG gel samples. The normalization concentration, ϕ_{ol} was taken as the 2D overlap concentration based on the estimated radius of gyration in theta solvent. Error bars represent standard error (S.E.) of the mean. The inset in (C) graphically depicts the definition of single (top), double (center), and triple (bottom) links between two crosslinks. (D) The probability distribution function (PDF) of attached chains' end-to-end lengths is shown for $\phi^* = 0.48$ (red), $\phi^* = 0.79$ (blue), and $\phi^* = 1.58$ (black) corresponding to the snapshots depicted in (A) from left to right, respectively. The mean lengths $\langle r \rangle$ are denoted by the vertical dotted lines of the same respective colors. (E) The RDFs of crosslink positions, $g(r)$, from the model are shown for $\phi^* = 0.48$ (red), $\phi^* = 0.79$ (blue), and $\phi^* = 1.58$ (black). (F) Mean clustering coefficient, $\langle C \rangle$, is plotted with respect to ϕ^*.

4.2. Gelation and as-prepared network topology

Here we demonstrate the model's *ab initio* reproduction of 10k tetra-PEG gel topologies based on as-prepared conditions. Initial gelation was carried out via the implementation outlined in Section 3.2 for networks swept across a range of as-prepared polymer concentrations (Fig. 9A,C), here characterized by $\phi^* = \phi/\phi_{ol}$, where ϕ_{ol} is the 2D overlap concentration of macromers estimated by $\phi_{ol} = fNbw/(2\pi R_g^2)$, and $R_g \sim Nf^{1/2}b^2$ is a star-shaped macromer's radius of gyration (see Appendix B for details). Bond attachment events were allowed to take place until the fraction of attached chains reached 0.95, tantamount to a high conversion during gelation as seen in experimental studies on tetra-PEG networks (Shibayama et al., 2019). Fig. 9B,C depicts the fraction of chains comprising single links and double links with respect to concentration. Here a "single link" is defined as a connection between crosslinks that share only one chain, while a "double link" or "triple link" (fraction not shown in Fig. 9C) indicates that the pair shares two or three chains, respectively. Such defects are critical in the accurate prediction of network mechanics and failure (Chung et al., 1996). Therefore, accurate replication of initial experimental gel topologies is crucial.

The trends in defect prevalence with respect to as-prepared concentrations strongly agree between the model and experiments. Higher as-prepared concentrations consistently result in networks with higher fractions of single links and fewer defects (e.g., double or triple links). While at a given as-prepared concentration the predicted fraction of single links is slightly higher (and the fraction of attached double links is lower) for the *in silico* experiments (Fig. 9C) than for experimental results (Fig. 9B) (Asai et al., 2013; Lange et al., 2011), this mismatch occurs primarily at higher concentrations and may be decreased by adjusting the timescale of Kuhn segment diffusion, τ_0 through Eq. (21). Additionally, the 2D overlap concentration estimated for simulations, is not synonymous with the rheologically extrapolated 3D overlap concentration cited by Lange et al. (2011), thereby rendering direct quantitative comparison between the horizontal axes of Fig. 9B,C uncertain. Ultimately, for the eventual purposes of predictive design, it is the relative trends in emergent topologies and mechanical properties that will guide fabrication parameters. Notably, at low concentrations a crossover region occurs for both simulations and experiments in which the fraction of double links becomes statistically consistent with that of single links, each representing between 40 and 50% of the overall population. However, for simulated gels prepared at $\phi^* \leq 0.5$, no networks formed (i.e., gelation was not observed), which is not consistent with the observations of Lange et al. (2011). As such, this iteration of the framework is limited to the study of sol-gels prepared at relatively high initial concentrations ($\phi^* > 0.5$). In future work this limitation may be overcome by introducing Brownian diffusion of entire macromers to emulate intervention mixing, however here

we focus on the case of gels fabricated at $\phi^* \sim 1.5$ (as depicted in the rightmost schematic from Fig. 9A).

For simulated gels prepared at $\phi^* \sim 1.5$ the mean end-to-end length of an attached chain is $\langle r \rangle = 12.1 \pm 0.1$ nm, or 28% of the overall contour length (Fig. 9D). Of note is that $\langle r \rangle$ changes little at lower concentrations ($\langle r \rangle = 13.6 \pm 0.1$ nm for $\phi^* \sim 0.8$ and $\langle r \rangle = 12.9 \pm 0.1$ nm for $\phi^* \sim 0.5$) (Fig. 9D) despite an obvious increase in effective mesh size as visually seen in Fig. 9A. This suggests that at lower concentrations, chains still relax to approximately the same lengths, but that crosslinks are generally more clustered (as indicated by the higher degree of double link defects from Fig. 9B,C), which is what enables a larger pore structure. Unlike the distributions of attached chain length, the RDF of crosslinks, $g(r)$, elucidates information about clustering (Fig. 9E). As expected, the RDFs universally indicate that the gels are amorphous, with high structural noise and no long-range order (Fig. 9E). However, at all three concentrations observed, there exists a length scale (~ 10 nm for $\phi^* \sim 1.5$, ~ 15 nm for $\phi^* \sim 0.8$, and $\sim 20 - 25$ nm for $\phi^* \sim 0.5$) below which the positions of crosslinks are highly correlated. This is consistent with the findings of Matsunaga et al. (2009b) and indicates the presence of clusters whose characteristic sizes are on the same order as these correlation lengths, suggesting that lower as-prepared concentrations beget larger clusters. Clustering is further characterized with respect to ϕ^* by the average clustering coefficient, $\langle C \rangle = \mathscr{N}^{-1} \sum_{\alpha} C_\alpha$ where $C_\alpha = 2T_\alpha / [k_\alpha (k_\alpha - 1)]$, k_α is the number of uniquely attached neighbors to crosslink α, T_α is the number of shared chains between said neighbors, and $k_\alpha (k_\alpha - 1)/2$ constitutes the number of possible shared connections between said neighbors (Soffer and Vázquez, 2005). $\langle C \rangle$ characterizes the extent to which attached neighbors of crosslinks are attached to one another thereby quantifying the degree of clustering. Fig. 9F demonstrates that $\langle C \rangle$ decreases as the as-prepared network concentration increases, supporting the interpretation that lower density networks exhibit greater clustering. Clusters are visible in Fig. 9A as the high osmotic pressure regions for $\phi^* \sim 1.5$ or the regions of high crosslink density for $\phi^* \sim 0.8$ and $\phi^* \sim 0.5$.

As an aside, below the length scale of 1.3 nm (for $\phi^* \sim 1.5$), $g(r)$ diverges suggesting that overlap of crosslinks occurs at the length scale of a Kuhn segment, which is a consequence of omitting any hard bodied repulsive potentials between nodes. While effective soft repulsion is introduced through the gradient in osmotic pressure, these forces are evidently overcome by the entropic tension of chains in some instances. Regardless, omitting hard body exclusion improves the numerical stability of the framework and only influences the displacement of crosslinks for gels by on the order of 1% of the contour length of a chain. Therefore, it has negligible effect on emergent network mechanics as revealed in the following sections.

4.3. Equilibrium swelling mechanics of gels

Having ensured that the initial topological features for the case of 10k tetra-PEG gels match available experimental data, we next examine the equilibrium swelling of percolated gels to ensure that their initial swelling behavior matches that predicted by the Flory-Rehner theory discussed in Section 2. For the purposes of this section, we use Gaussian (i.e., linear) chains and omit deterministic fracture of bonds. This allows us to use the relatively simple elastic strain energy density function of a compressible Neo-Hookean material given by:

$$\psi_{el} = \frac{\mu}{2}(\bar{I}_1 - 2) + \frac{\kappa}{2}(J-1)^2 \tag{31}$$

where μ is the shear modulus, κ is the bulk modulus, J is the Jacobian ($J = \det \boldsymbol{F} = \lambda_1 \lambda_2$), and $\bar{I}_1 = (\lambda_1^2 + \lambda_2^2)/\lambda_1 \lambda_2$ is the first invariant of the isochoric component of the left stretch tensor ($\bar{I}_1 = \mathrm{tr}\, \overline{\mathbf{B}} = \mathrm{tr}\, [J^{-1} \boldsymbol{F} \boldsymbol{F}^T]$ for symmetric deformation gradients). The maximum number of attachments per crosslink is relatively low ($f = 4$), so we set $\mu = (1 - 2/f) c k_b T$ in accordance with phantom chain theory for networks with low connectivity (Picu, 2011; Wagner et al., 2021). Here c is the network's attached chain concentration (Vernerey et al., 2017; Wagner et al., 2021), which evolves from the dry chain concentration (c_0) as the network undergoes volumetric deformation according to $c = J^{-1} c_0$. For reasons examined in Appendix C, we also posit that the bulk modulus, κ, evolves as $\kappa = 3\mu/2$ in 2D. To be consistent with the analysis of osmotic pressure, the reference state for J is taken as that of the dry polymer network.

Invoking the definition of Cauchy stress through Eq. (3), simplifying, and writing stress in terms of the principal stretch components gives:

$$\boldsymbol{\sigma} = \frac{2}{J}\left\{ \begin{bmatrix} \lambda_1/\lambda_2 & 0 \\ 0 & \lambda_2/\lambda_1 \end{bmatrix} - \frac{\lambda_1^2 + \lambda_2^2}{2\lambda_1 \lambda_2}[\boldsymbol{I}] \right\} + \frac{\kappa_0}{J}(\lambda_1 \lambda_2 - 1)[\boldsymbol{I}] \tag{32}$$

where $\kappa_0 = \frac{3}{2}(1 - 2/f) c_0 k_b T$ is the dry state bulk modulus. For the case of unconstrained (and therefore isotropic) swelling ($\lambda_1 = \lambda_2 = \lambda$), Eq. (32) reduces simply to $\boldsymbol{\sigma} = \sigma^h \boldsymbol{I}$ where:

$$\sigma^h = \frac{\kappa_0}{J}(J-1) \tag{33}$$

which represents the hydrostatic component of network stress, $\sigma^h = \mathrm{tr}(\boldsymbol{\sigma})/3$, and is plotted in Fig. 10A (black curve). Examining Fig. 10A, we see that σ^h increases monotonically with respect to J, and approaches a value of κ_0 in the limit $J \to \infty$. Notably, the form of σ^h presented through Eq. (32) is synonymous with that of the phenomenological, modified Ogden free energy functional introduced for rubberlike solids (Moerman et al., 2020; Ogden and Hill, 1972). This free energy formulation gives the hydrostatic stress as:

$$\sigma^h = \frac{\kappa}{J\beta}\left(1 - J^{-\beta}\right) \tag{34}$$

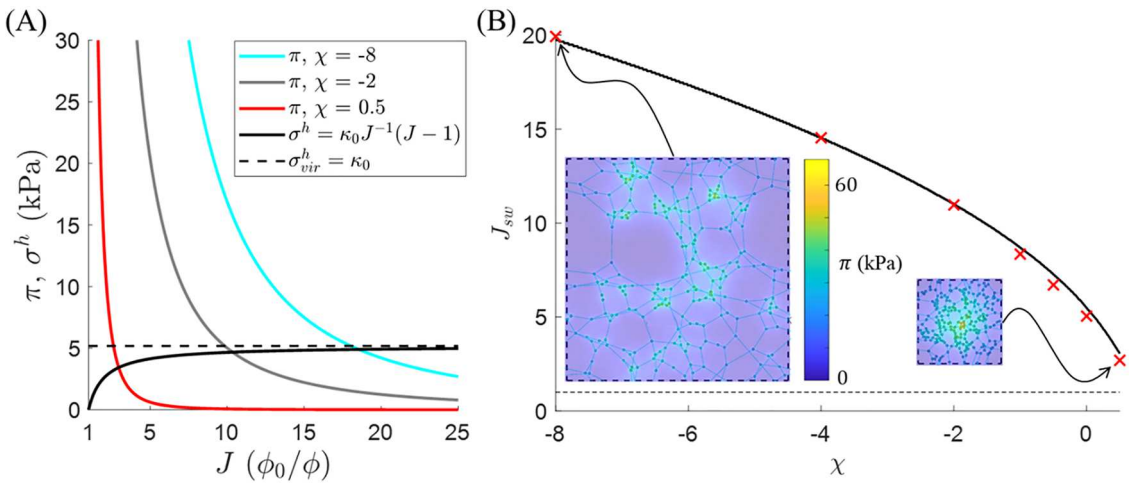

Fig. 10. Validation of the model's predicted swelling mechanics. (A) Osmotic pressure, π, is plotted as colored curves with respect to J for $\chi = 0.5$ (red), $\chi = -2$ (grey), and $\chi = -8$ (cyan). The hydrostatic component of network stress, σ^h, is also depicted for the modified Ogden model (black curve) in which $\kappa \propto J^{-1}$ (Moerman et al., 2020) and based on the virial formulation (dotted black curve). Where the colored curves and black curve intersect represents the equilibrium swell state per Flory-Rehner theory. (B) The continuous set of equilibrium swelling ratios from (A) are plotted with respect to $\chi \in [-8, 0.5]$. Discrete equilibrium swelling ratios (averaged over ten networks of linear springs with a functionality of $f = 8$) are plotted as red exes for the set $\chi \in \{-8, -4, -2, -1, -0.5, 0, 0.5\}$. S.E. of the mean constitutes less than 0.5% (or less than the marker size).

where κ is considered an invariant bulk modulus (i.e., is not a function of material density) and β is a material parameter governing the linearity of the system. Eqs. (33) and (34) are identical when $\beta = -1$. The invariance between σ^h and J for each of these formulations at high volumetric strains is perhaps intuitive if stress is contextualized as the free energy density of the elastic network. The free energy stored in the system increases proportionately to the stretch of the chains in each dimension ($\propto \lambda_1 \lambda_2 = J$), however the material density also decreases proportionately to volume ($\propto J^{-1}$), such that these two effects cancel one another. Indeed, the analytical virial formulation of network stress predicts complete invariance of σ^h with respect to J such that:

$$\sigma^h_{vir} = \kappa_0 \tag{35}$$

for networks whose only pairwise interactions are linear and tensile, even at low volumetric strains (Appendix C). Therefore, as illustrated in Fig. 10A, there is a notable discrepancy between σ^h_{vir} and σ_h at low values of J (e.g., approximately 40% difference when $J \approx 3$). Despite this, we find that numerically predicted values of σ^h are in good agreement with Eq. (35) for all values of J. This is likely due to the omission of volume exclusion interactions in the numerical model. At low volumetric strains, the hydrostatic stress response of a true material most likely increases more rapidly with respect to J due to the alleviation of repulsive forces between neighboring constituents as the material density declines. A reduction in repulsive forces corresponds to a reduction of pressure (not to be confused with "osmotic pressure") at the continuum scale. In turn, this drop in pressure amounts to an increase in hydrostatic stress as entropic chain forces become the dominant phenomenon. Thus, the modified Ogden model likely remains an accurate phenomenological predictor of materials' true stress responses and mismatch here derives from our deliberate choice to neglect volume exclusion interactions for simplification. Volume exclusion interactions may be easily included in future iterations of this model concerned with materials at higher densities.

To assess the effect of osmotic pressure on gel swelling, the mixing parameter was numerically swept over the arbitrary set, $\chi \in \{-8, -4, -2, -1, -0.5, 0, 0.5\}$, where $\chi < 0$ indicates that there is an effective repulsive potential between solute particles when placed in solvent (Doi, 2013). Fig. 10B depicts the swelling ratios J with respect to the mixing parameter χ, as predicted by Flory-Rehner theory (using the modified Ogden strain energy) and the discrete model (red scatterplot). The continuous curve in Fig. 10B may be graphically interpreted as the horizontal coordinates at which the χ-dependent osmotic pressure curves intersect the hydrostatic stress curve in Fig. 10A. Regardless of whether the virial formulation or modified Ogden model is used to predict σ^h, the numerical model predicts equilibrium swelling characteristics in good agreement with Flory-Rehner theory, even at low volumetric strains. This is because relatively large discrepancies in the equilibrium stress value (i.e., vertical axis intersection of curves in Fig. 10A) amount to relatively small changes in J at low strains Given the accurate prediction of swelling mechanics demonstrated here, in future studies, this model feature may be utilized in conjunction with force-sensitive bond dissociation to predict and avoid fabrication parameters that result in reverse gelation.

4.4. . Elastic response of a gel undergoing external load

While this model predicts swelling ratios in agreement with the predictions of Flory-Rehnner theory for networks of ideal chains, it

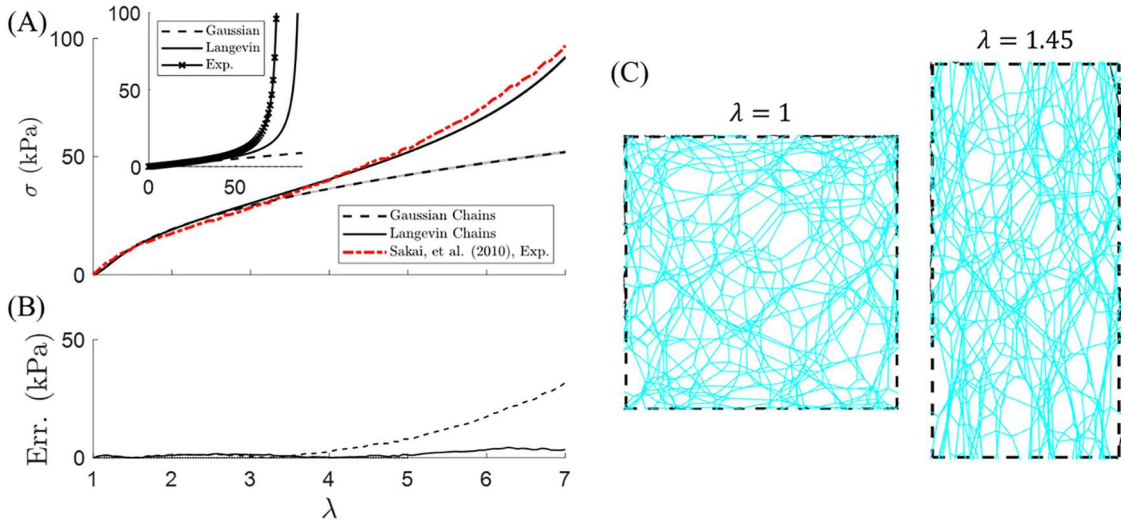

Fig. 11. Validation of the model's predicted stress response. (A) The principal component of nominal network stress in the direction of uniaxial extension is plotted with respect to stretch for 20k tetra-PEG gels. The experimental results (red dashes) of Sakai, et al. (2010), are plotted against model predictions for networks of Gaussian (dotted black) and Langevin (solid black) chains. The shaded regions for numerical results denote S.E. of the mean. The inset displays the force (pN) versus extension (nm) relationships for the Gaussian and Langevin chains ($L = 88$ nm) of the model, as well as the inversely derived experimental force-extension reported by Sakai, et al. (2010) ($L = 76$ nm). (B) Root mean square error (RMSE) is plotted with respect to stretch. (A-B) Share a horizontal axis. (C) Snapshots of a numerical network at stretches of $\lambda = 1$ and $\lambda = 1.45$ are depicted for reference.

is also important to validate its prediction of mechanical response against nonlinear experimental results. We here demonstrate that the model's prediction of stress-stretch response ($\sigma - \lambda$) is in agreement with the experimental results presented by Sakai et al. (2010) for 20k tetra-PEG gels undergoing uniaxial extension (Fig. 11). 20k tetra-functional networks comprised of Langevin chains were generated per the methods of Section 3, however equilibrium swelling was not conducted. Instead, after percolation (i.e., continuous network formation), the initial RVE domain size was adjusted until the initial mean attached chain length $\langle r \rangle$ was within 5% of the initial chain length ($r_0 = 7.1$ nm) reported experimentally, thereby ensuring that λ is reported with respect to the same reference state for both numerical and experimental results. To match experimental loading conditions, incompressible uniaxial tension was applied through the deformation gradient $\boldsymbol{F} = \mathrm{diag}(\lambda^{-1}, \lambda)$. To fit the model's 2D predicted stress-stretch behavior against 3D experimental results, we invoke plane stress boundary conditions (i.e., stress-free boundaries on the faces whose norms are out-of-plane), for which a tertiary dimension (i.e., the RVE thickness, ζ) is needed to meaningfully compute the virial stress.

As illustrated in Fig. 11A, the results of our model agree reasonably well with the experimental results when said thickness is set to $\zeta = 7.4$ nm, which approximately coincides with the initial mean chain end-to-end length of $\langle r \rangle \approx 7.5$ nm, suggesting that the numerical RVE represents one layer of crosslinks. To emphasize the importance of finite chain extensibility, Fig. 11 includes predicted results using both linear (Gaussian) and nonlinear (Langevin) chains. We see that for linear networks the model quickly deviates from the experimental stress-stretch behavior reported, whereas low error (RMSE < 1.5 kPa) is achieved when Langevin chains are used in the regime $\lambda \leq 5$ (Fig. 11B). Error reaches up to RMSE$\approx$ 6 kPa or $\sim$6–10% of the overall network stress for $\lambda > 5$. However, this is attributed to earlier divergence of the force-extension relation (occurring when $r \to L$) reported by Sakai et al. (2010), than that used in the model. The single chain force-extension relations of both works are displayed in the inset of Fig. 11A. Note that for the number of macromers modeled ($\mathcal{N} = 625$) the domain width became smaller than that of a single chain's contour length above $\lambda = 7$, hence the upper limit of stretch reported.

5. Damage and the role of heterogeneities

Given the accurate predictions of network topology, swelling mechanics, and stress response for 10k and 20k tetra-PEG gels thus far, the remainder of this work is devoted to using the model to extrapolate predicted mechanical properties of gels across a range of functionalities and molecular weights (or chain contour lengths). It is well documented that the damage of polymeric materials, including gels is sensitive to defects and thus topology (Jangizehi et al., 2020; Kothari et al., 2018; Sanoja et al., 2021; Vernerey et al., 2018). Therefore, in Section 5.1, we examine the predicted mechanical properties and failure mechanics of four network types (representing two functionalities and two chain lengths). We then quantify topological properties and visually inspect the network configurations to explain the observed trends. In Section 5.2, we conduct a larger parameter sweep and introduce a set of structure-property function plots that aid in understanding the role of topology on mechanical failure.

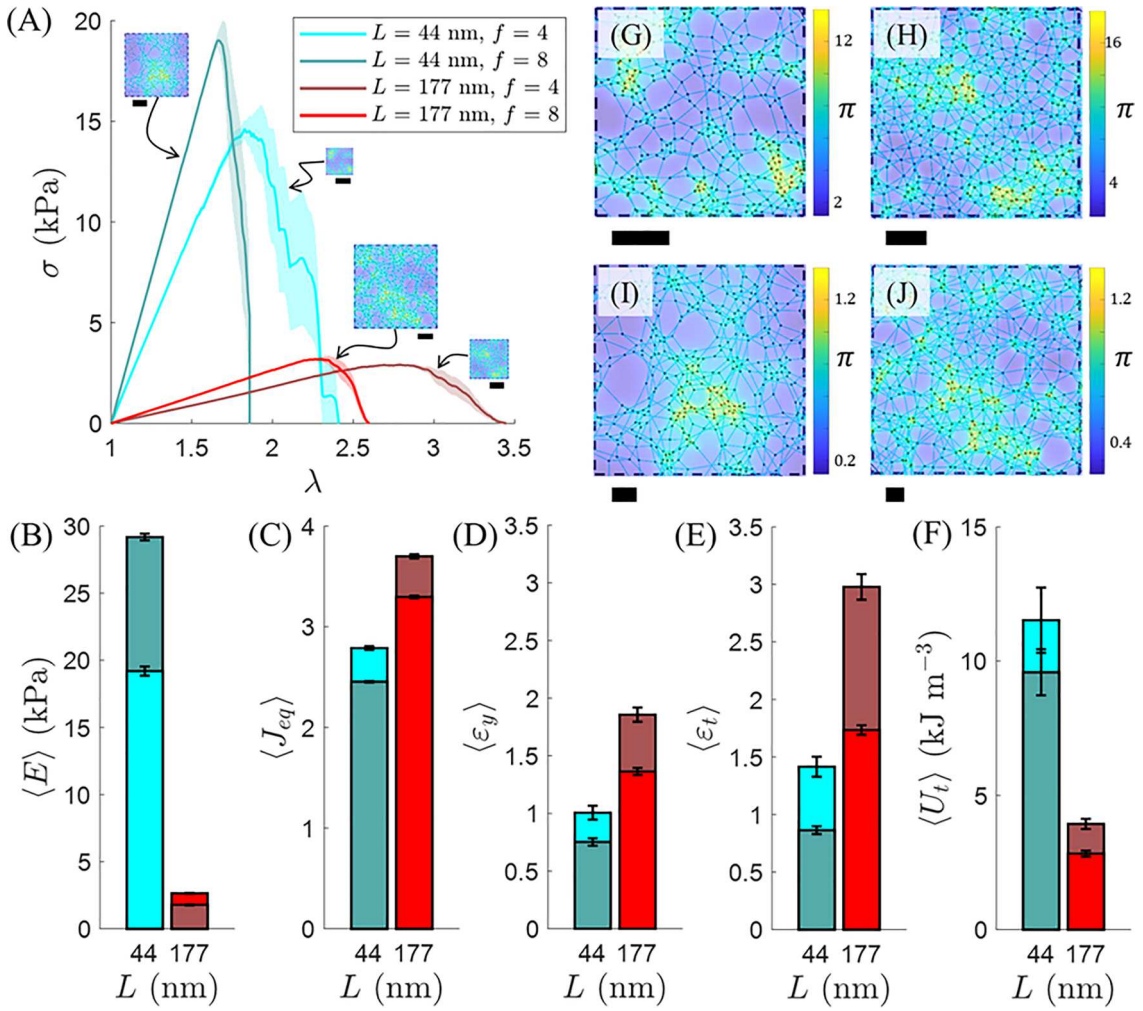

Fig. 12. Mechanical predictions of gels with different functionalities and chain lengths. (A) The ensemble averaged principal component of Cauchy network stress in the direction of uniaxial extension from ten simulations ($n = 10$) is plotted with respect to stretch measured from the equilibrated swollen state. This relation is shown for four types of tetra-PEG gels with varying chain contour lengths L and functionalities f as indicated by the legend. The inset snapshots depict sample networks for each combination of L and f, all at the same length scale to emphasize the different degrees of initial chain stretch, which results from different dry macromer densities (based on functionality) and initial swelling ratios. The average (B) tangent modulus $\langle E \rangle$, (C) equilibrium swell ratio $\langle J_{eq} \rangle$, (D) strain at peak force $\langle \varepsilon_y \rangle$, (E) failure strain $\langle \varepsilon_t \rangle$, and (F) toughness $\langle U_t \rangle$ are displayed for each chain contour length and functionality. Colors correspond to the legend from (A). (G–J) Close-up views of the snapshots from (A) are depicted for the networks with (G) $L = 44$ nm and $f = 4$; (H) $L = 44$ nm and $f = 8$; (I) $L = 177$ nm and $f = 4$; and (J) $L = 177$ nm and $f = 8$. All shaded regions or error bars represent S.E. of the mean. All scale bars represent 50 nm. Heat maps represent osmotic pressure.

Table 2
Macromer inputs for the networks of Fig. 12.

Network No.	Molecular Weight, M_w (kDa)	Chain Contour Length, L (nm)	Functionality, f
1 (Blue)	10	44	4
2 (Teal)	20	44	8
3 (Maroon)	40	177	4
4 (Red)	80	177	8

5.1. *Mechanical and topological properties of ab initio tetra-PEG gels*

Fig. 12 presents the predicted stress-stretch response and mechanical properties of tetra-PEG gels with the combinations of M_w (or L) and f indicated in Table 2. Damage was introduced using the deterministic failure criteria used by Sugimura et al. (2013), whereby scission occurs for chains whose end-to-end lengths reach 95% of their contour lengths. Although enthalpic bond stretching becomes a

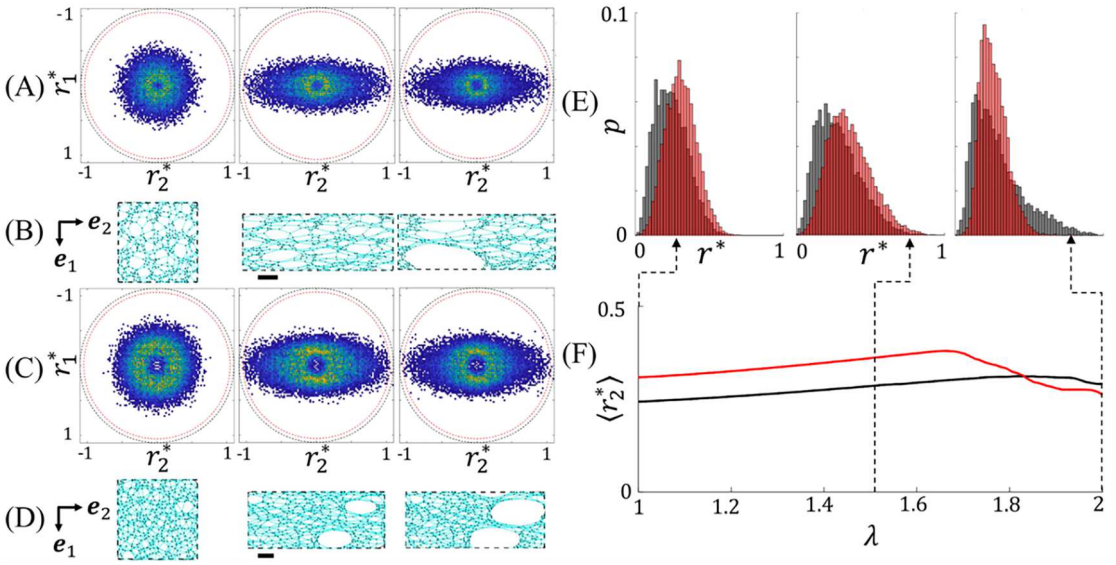

Fig. 13. Chain distribution functions of gels with $L = 44$ nm and different functionalities. (A) The joint PDF of r^* is shown for the ensemble of ten ($n = 10$) 10k tetra-PEG gels at $\lambda = 1$ (left), the measured yield stretch $\lambda = 2.00$ (center), and the measured failure stretch $\lambda = 2.16$ (right). (B) Snapshots of a sample 10k tetra-PEG network at the stretches from (A) are depicted. The network depicted did not reach absolute failure by the average failure stretch of $\lambda = 2.16$. (C) The joint PDF of r^* is shown for the ensemble of ten 20k octa-PEG gels at $\lambda = 1$ (left), the measured yield stretch $\lambda = 1.75$ (center), and the measured failure stretch $\lambda = 1.83$ (right). (D) Snapshots of a sample 20k octa-PEG network at the stretches from (C) are depicted. The network depicted did not reach absolute failure by the average failure stretch of $\lambda = 1.83$. (A–D) The extensile direction, $\boldsymbol{e}_2$ is oriented horizontally. Scale bars in (B) and (D) represent $L = 44$ nm. Dashed black circles in (A) and (C) indicate the chain contour length, while dashed red circles represent the deterministic scission length for chains. (E) The radial PDFs of r^* are shown for the 10k tetra- and 20k octa-PEG gels as grey and red histograms, respectively. For direct comparison, these histograms are depicted at $\lambda = 0$ (left), $\lambda = 1.5$ (center), and $\lambda = 2.0$. Note that the chains in these two networks have the same contour length. (F) The average component of normalized chain end-to-end length in the principal direction of extension is plotted with respect to stretch. End-to-end lengths are normalized as $r^* = r/L$ such that $r^* \geq 0.95$ prompts chain scission.

significant effect influencing the failure of polymer chains at high strains (Lamont et al., 2021), it demonstrably increases the stiffness of PEG chains in water by multiple orders of magnitude (Ahlawat et al., 2021; Oesterhelt et al., 1999). As such, the exact stretch at which carbon-carbon binding energy is exceeded (i.e., rupture occurs) will reside near $\lambda \to \sqrt{N}$, hence the use of this coarse failure criteria for our purposes. As one would expect, from Fig. 12A we see that increasing the contour lengths of chains resulted in softer networks (i.e., lower Young's moduli, E, Fig. 12B) that therefore reach larger equilibrium swelling ratios (J_{eq}, Fig. 12C) and higher deformations prior to yield (Fig. 12D) and failure (Fig. 12E). Perhaps unexpectedly, these networks absorbed less energy prior to fully fracturing (i.e., exhibited lower toughness, U_t, taken as $U_t = \int \sigma(\varepsilon) d\varepsilon$ in the limits ε_{eq} to ε_t) (Fig. 12F). However, this is partially realized by the fact that longer chains store less mechanical energy at a given stretch, thus reducing the strain energy density of the overall network. Furthermore, here ε was measured from the swollen equilibrium state, as opposed to the dry state or ideal chain end-to-end length ($\langle r \rangle = b\sqrt{N}$). Since the networks made from longer chains begin at a higher swelling ratios, their chains begin at higher effective stretches. Visually, this is illustrated by both the inset depictions of the initial networks in Fig. 12A, which are all depicted at the same length scale, as well as the close-up snapshots of these same networks from Fig. 12G–J, whose scale bars all represent 50 nm. Despite significant differences in initial chains stretch in the equilibrated swollen states, the lower limit used to compute U_t was always taken as $\varepsilon_{eq} = \sqrt{J_{sw}} - 1$. This lower limit choice also explains why the networks with chains that are roughly four times longer (177 versus 44 nm) are not four times as extensible (Fig. 12E).

Also as expected, increasing the functionality of networks with the same length chains stiffened them (i.e., increased E), thereby decreasing J_{eq} and increasing peak stresses (σ_y) (Fig. 12A). This is because introducing a higher crosslink density to the network ensures that more chains may effectively carry load in parallel. However, less intuitively, as seen from Fig. 12D–F, increasing functionality also resulted in a decrease of the strain at peak force (ε_y, taken as the average strain at which stress peaks), fracture strain (ε_t), and therefore toughness (U_t) of the networks, indicating more brittle behavior. To explain this behavior from a micromechanical perspective, we must understand how the chains in these respective networks are oriented and stretched prior to and during deformation.

Fig. 13A and C depict the joint probability distribution functions of the normalized chain end-to-end lengths $r^* = r/L$ for 10k tetra- and octa-PEG gels, respectively. Examining Fig. 13A–E, it is immediately apparent that a greater fraction of the chains in the octa-PEG network exists at higher values of r^*, even prior to deformation. Plotting the average value of r^* in the principal direction of extension, $\langle r_2^* \rangle$, against λ for each network (Fig. 13F) confirms that the mean end-to-end length of chains in the octa-PEG gel is almost universally higher in the stretch regime $1 < \lambda < 1.8$ than those in the tetra-PEG gel. Indeed, $\langle r_2^* \rangle$ is only lower for the octa-PEG network in this range of λ after the gel fully fractures ($\lambda > 1.83$). Visually investigating the networks at their initial state immediately elucidates an

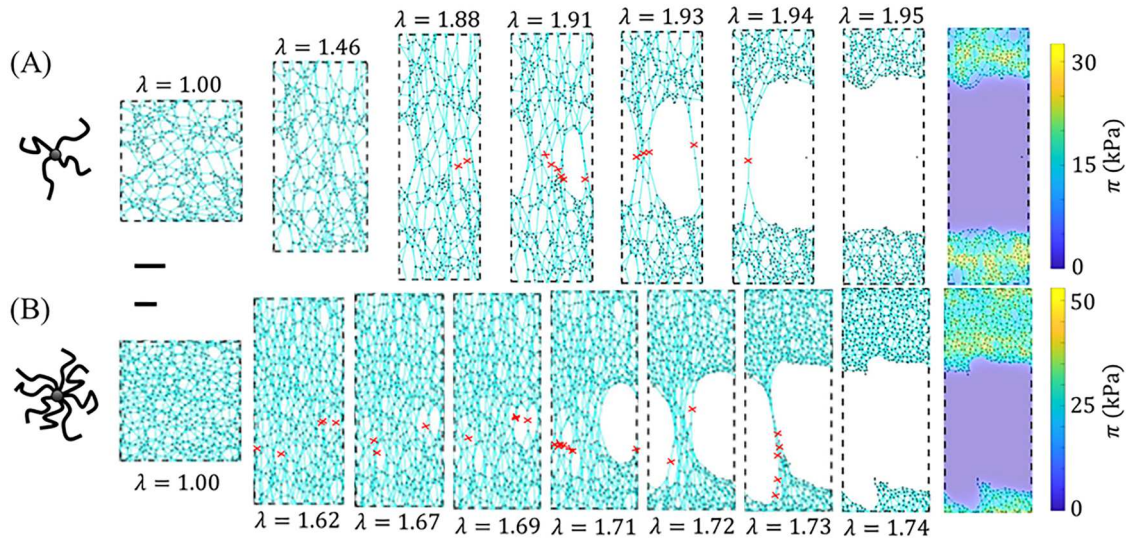

Fig. 14. Fracture of gels with $L = 44$ nm and different functionalities. (A) A schematic of a tetra-functional macromer is depicted, alongside snapshots of a simulated 10k tetra-PEG gel as it undergoes uniaxial extension. (B) A schematic of an octa-functional macromer is depicted, alongside snapshots of a simulated 20k octa-PEG gel as it undergoes uniaxial extension. The macromer schematics are depicted at the same scale, whereas the sizes of the gel snapshots are indicated by their respective scale bars, each representing L. Red crosses in the gel snapshots demark which chains rupture before the next displayed snapshot. The rightmost snapshots depict the osmotic pressure landscapes of the domains at initial fracture.

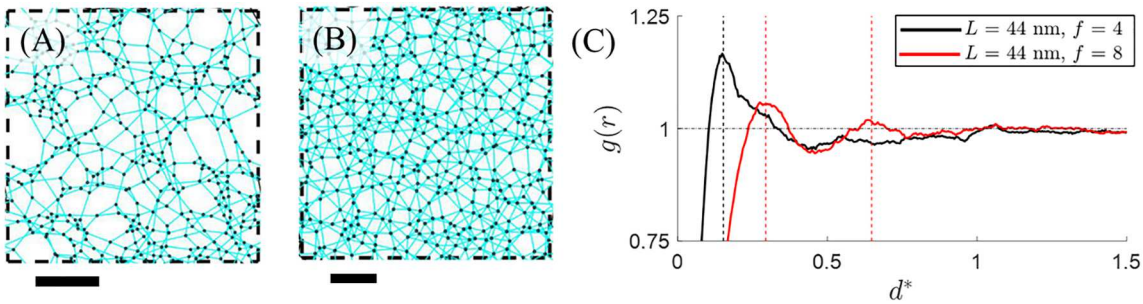

Fig. 15. RDFs of gel's crosslinks with $L = 44$ nm and different functionalities. (A,B) Samples of a (A) 10k tetra-PEG and (B) 20k octa-PEG networks are shown at $\lambda = 1$ for visual reference. Scale bars represent $L = 44$ nm. (C) The RDFs of ensembles of ten ($n = 10$) 10k tetra-PEG (black) and ten 20k octa-PEG (red) gels' crosslinks are displayed. The distance between crosslinks is normalized as $d^* = d/L$. Dotted lines denote correlation length scales or peaks in $g(r)$.

obvious cause of this. Fig. 14A and B, illustrates samples of simulated 10k tetra-PEG and 20k octa-PEG gels, respectively, at various uniaxial stretches up to full fracture. Each network was generated from the same number of macromers ($\mathcal{N} = 400$), and we know from Fig. 12C that the 10k tetra-PEG network has swelled more from its initial dry state to the references state shown. Despite this, the scale bar (which represents L) is 38% larger for the 10k tetra-PEG gel (Fig. 14A) than it is for the 20k octa-PEG gel (Fig. 14B). This is because the 20k octa-PEG gel occupies more space per macromer in its dry state than the 10k tetra-PEG gel, simply because it has a greater number of chains, a notion made visually apparent by the macromer illustrations in Fig. 14. Were the topological features of these networks (such as coordination number and variance of the end-to-end length) equal, then this difference in swelled dimensions would immediately imply that the chains in the 20k octa-PEG gel begin at a 38% greater stretch prior to deformation, closely reflecting the average 39.8% greater extensibility of the 10k tetra-PEG gels.

However, the topological properties in these two gels are not the same, with the 20k octa-PEG gel appearing more homogenized (Fig. 15A,B). This is reflected in the radial distribution functions (RDFs) at $\lambda = 1$ displayed in Fig. 15C, which reveal that the 10k tetra-PEG gel displays just one correlation length scale around $d^* = 0.15$ followed by an inversely correlated region from $d^* \approx 0.3$ to $d^* \approx 1$ (i.e., $g(0.3 \leq d^* \leq 1) < 1$). The single correlation peak indicates that crosslinks in the lower functionality network are relatively clustered in regions wherein the most common pairwise separation is approximately 15% of L. The inversely correlated regime indicates that clusters are separated by vacant regions with a characteristic size on the order of L. This is visually supported by the network depicted in Fig. 15A. In contrast, the RDF of the 20k octa-PEG gel displays two correlation length scales (i.e., peaks) around $d^* = 0.29$ and 0.65, indicative of more ordered crosslink distribution below $d^* = 1$ and greater homogeneity of the higher functionality

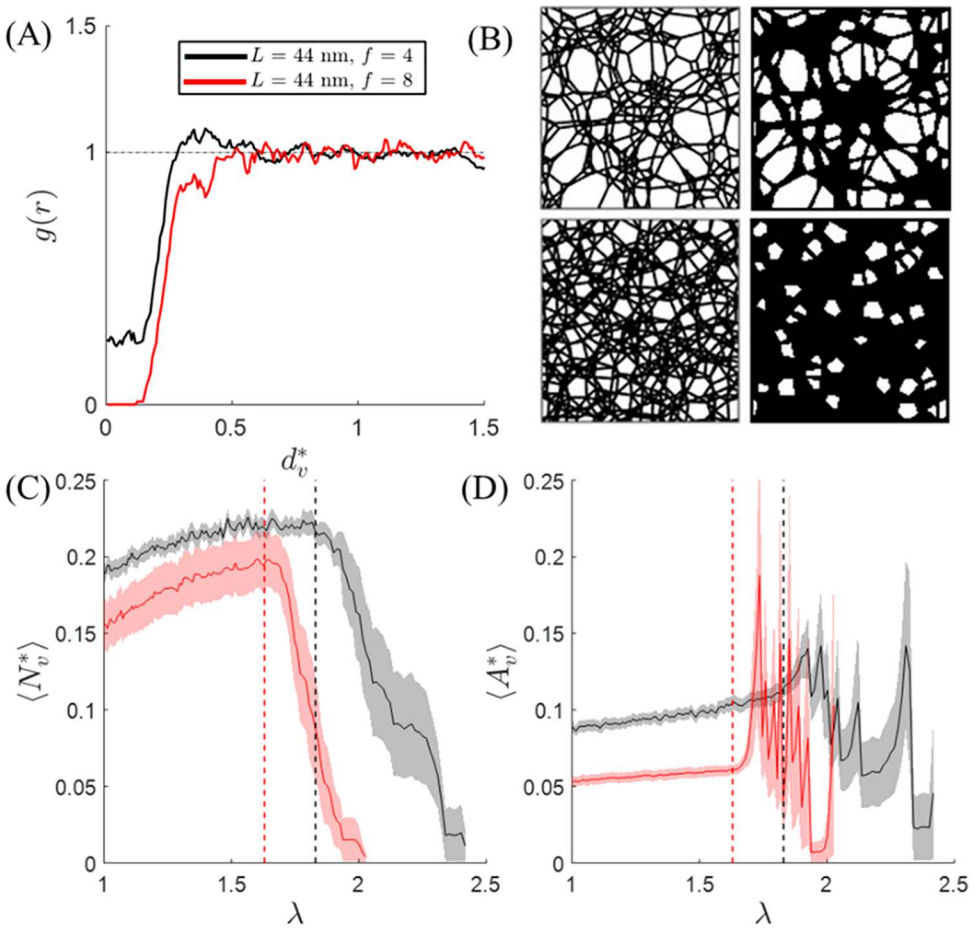

Fig. 16. Void characteristics of gels with $L = 44$ nm and different functionalities. (A) The RDFs of ensembles of ten ($n = 10$) 10k tetra-PEG (black) and ten 20k octa-PEG (red) gels' void centroids are displayed at $\lambda = 1$. The distance between void centroids is normalized as $d_v^* = d_v / L$. (B) Black-white snapshots of sample networks are displayed. The left column displays the black-white network configurations of a 10k tetra-PEG gel (top) and 20k octa-PEG gel (bottom) prior to deformation. The right column displays the same respective networks with pores below the prescribed threshold filtered out (to reduce noise). (C) The average number of voids per macromer is plotted with respect to stretch. (D) The average void area (normalized as $A_v^* = A_v / \pi L^2$) is plotted with respect to stretch. (C,D) Shaded regions represent S.E. of the mean. The vertical dotted lines denote the approximate stretches at which bond rupture events were first detected through Fig. 14 ($\lambda \approx 1.85$ - black, $\lambda \approx 1.6$ - red).

gel. One clear, inversely correlated region exists for the 10k tetra-PEG gel in the approximate range $0.4 < d^* < 0.6$, indicating a smaller characteristic size of vacant regions, which is visually illustrated by Fig. 15B. While one might assume that this results in greater resistance to damage, it merely promotes the nucleation of more numerous, but smaller voids as bond scissions begin. This is somewhat reflected by the red crosses in the network snapshots Fig. 14, which demark the bonds that rupture in each subsequent frame. We see that the first discrete rupture events occur in wholly separate regions of the 20k octa-PEG gel (see $\lambda = 1.62$ or 1.67), whereas the first rupture events of the 10k tetra-PEG gel (see $\lambda = 1.88$) are localized to one region that already exhibited low chain density.

To gain a quantitative understanding of damage onset, we utilize image analysis to measure and plot the RDF of void centroids, as well as the average number of voids and void area with respect to stretch for the gels with $L = 44$ nm (Fig. 16). To remove noise and filter out pores occurring in highly clustered regions, we define "voids" simply as pores in the network whose areal size is greater than $A_v = 0.25\pi\rho^2$ where $\rho = 0.15$ is the shortest correlation peak length scale measured from Fig. 15C. The RDFs of Fig. 16A reveal that void positions are not correlated in either network above a lengths scale of $d^* \sim 0.5$. However, the voids in the tetra-functional network are demonstrably more clustered with some small correlation existing around $d^* \sim 0.3$ and a non-negligible population of voids within less than $d^* \sim 0.2$ of one another. This supports the greater homogeneity of the octa-functional gels and is made visually clear by the black and white network depictions in Fig. 16B both without (left) and with (right) filtration of small pores. Examining the statistics of voids during deformation, Fig. 16C and D indicate that the average number of voids per crosslink $\langle N_v^* \rangle$ and average void area $\langle A_v^* \rangle$ (normalized as $A_v^* = A_v / 0.25\pi L^2$, where $0.25\pi L^2$ is the maximum envelope of a single macromer) are both consistently higher for the tetra-PEG gel than the octa-PEG gel, which is perhaps trivial. Of note though is that the first observed instances of rupture events (denoted by the vertical dotted lines in Fig. 16C,D) are closely followed by steep declines and spikes in $\langle N_v^* \rangle$ and $\langle A_v^* \rangle$, respectively,

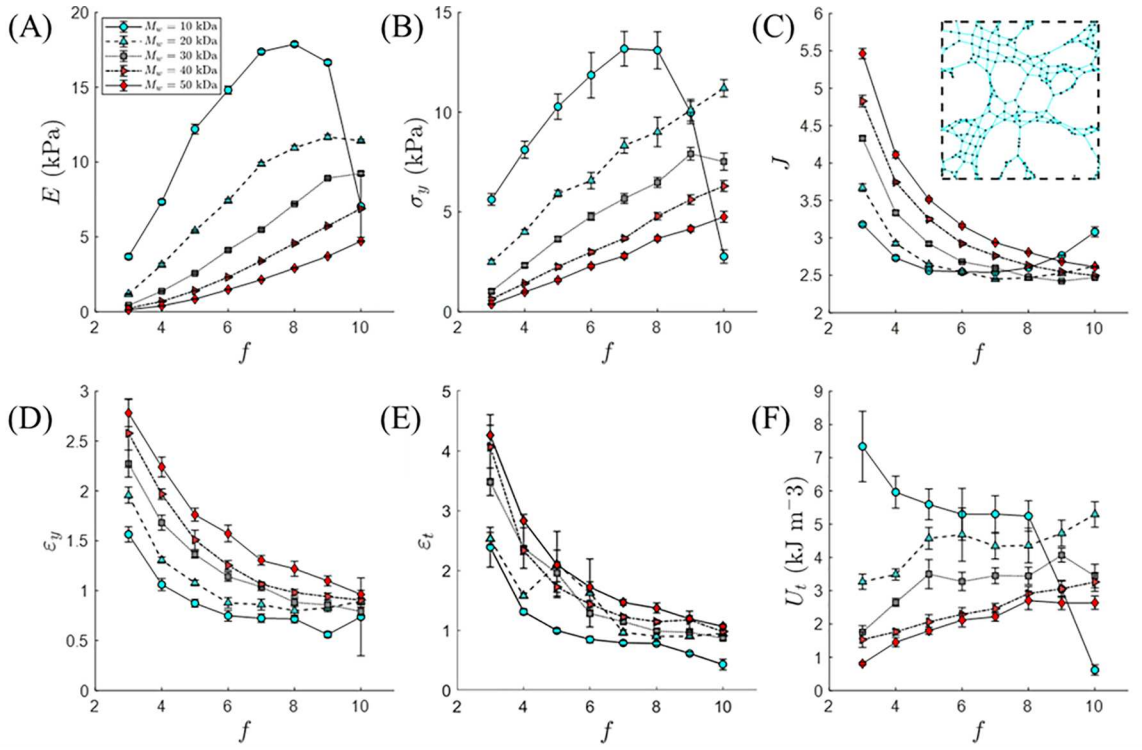

Fig. 17. Mechanical predictions for extended parameter sweep. Mean (A) Young's modulus, (B) peak stress, (C) equilibrium swell ratio, (D) strain at peak stress, (E) failure strain, and (F) toughness are plotted with respect to functionality for $M_w = 10$ kDa (blue circles), $M_w = 20$ kDa (teal triangles), $M_w = 30$ kDa (grey squares), $M_w = 40$ kDa (sideways maroon triangles), and $M_w = 50$ kDa (red diamonds). Ten ($n = 10$) samples of each network type were modeled. Error bars represent S.E. of the mean. The inset of (C) displays the anomalous topology of a gel with $M_w = 10$ kDa and $f = 10$, as discussed in the main body text.

quantifying the rapid void coalescence illustrated through Fig. 14. Note that subsequent drops in $\langle A_v^* \rangle$ are due to elastic energy in the network causing local retraction around highly damaged regions, thus restoring a smaller average pore size. However, it must be noted that without inclusion of a fluid transport timescale, the rate of this elastic retraction is likely misrepresented by this iteration of the model, as reflected by the high disparity in osmotic pore pressure between the fractured and intact network domains (see the rightmost panels of Fig. 14). Poroelastically slowed retraction around damage zones may mitigate the onset of stress risers that result from heightened strain of one or a few intact chains, thus perhaps also delaying the rate of crack propagation in true gels. In future iterations of this approach, we will incorporate poroelasticity via a fluid transport timescale and investigate this likelihood. Nonetheless, this iteration of the model is still revealing regarding damage initiation as it relates to the *ab initio* inputs.

No statistically significant difference was measured between the average rate at which voids initiate ($\partial \langle N_v^* \rangle / \partial \lambda$), nor the rate at which their average area increases ($\partial \langle A_v^* \rangle / \partial \lambda$) prior to damage onset ($\lambda < 1.5$). Nevertheless, it is clear from this analysis that the higher functionality leads to a more homogenous domain with fewer and smaller voids. Thus, while the lower failure strains of higher functionality networks are attributed primarily to the higher initial stretch of the chains therein, it is also likely that brittle behavior is exacerbated by a higher degree of load sharing and homogeneity between chains as they approach their failure criteria (here, $r^* \to 0.95$, but governed by bond dissociation energy in true polymer chains (Eyring, 1935)) This culminates in greater homogeneity of the subsequent failure domains and rapid void coalescence. This analysis holds true in comparing the 40k tetra-PEG gels to 80k octa-PEG gels (both of which have $L = 177$ nm), as well (see Appendix D for extended data).

5.2. Predictive mapping as functions of M_w and f

Having postulated micromechanical causes of observed trends in emergent properties, we here conduct a broader parameter sweep to predict high order mechanical trends in PEG-based gels. Fig. 17 plots mean values of Young's modulus (E), peak stress (σ_y), swell ratio at initial equilibrium (J), strain at peak stress (ε_y), failure strain (ε_t), and toughness (U_t) with respect to $f \in [3, 10]$, for five different molecular weights ($M_w \in \{10, 20, 30, 40, 50\}$ kDa). While PEG-based copolymers with $f \in \{2, 4, 8\}$ are perhaps most typical, we include uncommon functionalities to highlight the mechanical trends and with the recognition that intermediate effective functionalities are attainable contingent on network composition (Schultz et al., 2009). We exclude systems in which $f = 2$ as these are below the percolation threshold. Note that we no longer set M_w to fix the chain length based on functionality, as we are now interested in examining the effects of typical control parameters used by experimentalists.

The mechanical trends are in general agreement with existing literature (Matsunaga et al., 2009a; Sun et al., 2008; Temenoff et al., 2002). Greater M_w typically decreases the elastic modulus (Fig. 17A) and yield stress (Fig. 17B) of the networks due to the increased length and decreased stiffness of the chains (thereby increasing the equilibrium swelling ratio - Fig. 17C). In contrast, greater M_w increases the yield (Fig. 17D) and failure strains (Fig. 17E) of networks due to the increased extensibility of the underlying chains. It appears that the decreases in moduli robustly outpace the increases in extensibilities and result in an overall decrease in dissipated energy upon failure (i.e., toughness) with respect to M_w (Fig. 17F). Regarding network connectivity, greater f generally increases modulus (Fig. 17A) and yield stress (Fig. 17B) thereby decreasing equilibrium swelling ratio (Fig. 17C), due to the increased stiffness associated with higher chain concentrations. Given increased network homogeneity and initial chain stretch (as discussed in Section 5.1), greater f also generally decreases the strains at peak stresss and failure (Fig. 17C,D). Interestingly, the toughness (Fig. 17F) appears to either decrease or increase with respect to f depending on M_w. Specifically, the toughness of networks generated using $M_w = 10$ kDa increases as f decreases, whereas toughness appears positively correlated with f for all other values of M_w investigated. Notably, the toughness of gels with intermediate functionalities ($5 \leq f \leq 8$) and low molecular weights ($M_w \leq 30$ kDa) does not vary significantly with respect to f given the number of samples ($n = 10$) observed. Despite the significance of functionality's impact on mechanics, existing experimental literature examining its specific effects on star-polymer-initiated networks' mechanical properties was not identified in the context of PEG gels (unless significant compositional changes were involved as in the studies of (Schultz et al., 2009)). Nevertheless, further investigation is justified, and functionality will be central to the scope of forthcoming studies in which we probe the mechanical properties of both tetra and octa-functional macromers comprising a covalently adaptable gel (Richardson et al., 2019).

While the overall trends observed here are largely in agreement with those observed by experimentalists, the limitations of extrapolated predictions are perhaps highlighted by the outlier case in which $M_w = 10$ kDa and $f = 10$. A precipitous drop in modulus, yield stress, and therefore toughness is observed for networks with these inputs. We see from Eq. (15) that the solute concentration (with respect to radial distance from a crosslink) scales proportionately to the functionality and inversely with the mesh size in the model ($\phi(r) \sim f/\bar{\xi}$). As such, through Eq. (18), high effective osmotic repulsive forces occur between macromers with these properties despite their short chain lengths (of 35 nm). Hence, during gelation, a high fraction of defects emerges as - at the as-prepared concentration - each macromer is more likely to double or triple link to a few nearest neighbors rather than bond equi-azimuthally with its surroundings. This yields gel topologies with high defect fractions as depicted in the inset of Fig. 17C. These defects soften the networks' mechanical responses (Lange et al., 2011). In truth, adequate mixing during gelation is generally facilitated in experiments by Brownian diffusion and stirring intervention (Shibayama et al., 2019), neither of which were modeled here. Therefore, future application of this method for the predictive design of experimental systems should commence with multiple model calibration experiments, preferably at the extreme ends of the relevant parameter space.

6. Concluding remarks

In this work we have introduced a theoretical and computational framework for modeling the spatial distribution of macromers in sol-gels, based on the nm-scale solute-concentration landscape and its effect on the local osmotic pressure gradient as dictated by Flory-Huggins mixing theory. The method constitutes a more physically motivated approach than the phenomenological, effective pairwise potentials often employed at the network scale to capture inter-polymer repulsion and depletion interactions. While the methods introduced here may be incorporated into 3D models, for simplicity, we initially incorporated them into a 2D, discrete numerical framework adopted from our previous work (Wagner et al., 2021). Indeed, both topological and mechanical properties may be affected by network dimensionality. For example, both network connectivity and degree of non-affine deformation tend to be larger in 3D networks (Picu, 2011), and so in future efforts we will apply these methods to 3D domains. Nevertheless, we here demonstrated this initial framework's prediction of mixing and phase separation as a function of the Flory mixing parameter, χ, thereby exhibiting its potential for use modeling polymer suspensions. As the primary focus of this work, we then demonstrated this framework's accurate *ab initio* prediction of the topological and mechanical properties of tetra-PEG gels as functions of their as-prepared polymer concentration, molecular weight, and functionality. Finally, we utilized the framework to extrapolate predicted mechanical properties of gels, further exploring the effects of molecular weight and functionality.

We found that increasing molecular weight generally decreased the moduli, yield stresses and toughness of gels. In contrast, it reliably increased their equilibrium swelling ratio, and their extensibility with respect to the swollen reference state. As expected, increasing the functionality of crosslinks also increased stiffness of the emergent gels; however, less intuitively increased functionality (given the same chain length and as-prepared concentration) decreased mechanical toughness and failure strains (as measured from the swollen state). We found that this was due primarily to higher initial stretch of the polymer chains for gels with higher chain concentration, emphasizing that the effects of initial swelling must be accounted for when designing the mechanical properties of gels. This greater initial swelling imposes residual stresses that result directly from increased functionality. This finding is consistent with that of Kothari et al. (2018) who reported that increasing crosslink density in mesoscopically modeled polymer networks reduced overall network extensibility due to higher pre-stressing of the chains. However, the approach introduced here is novel in its ability to explain such phenomena as governed by the *ab initio* sample preparation conditions that experimentalist can control. Nonetheless, there are two major advantages introduced through mesoscopic frameworks such as these. Firstly, they allow for the direct, detailed observation of local topological traits in a way that is unattainable through existing experimental characterization techniques or

continuum models. Secondly, they do so while mitigating much of the computational cost associated with modeling every polymer chain explicitly. Therefore, these methods are inherently more scalable than conventional coarse-grained MD models. Moving forward, the *ab initio* approach of this model may be used both to inversely investigate the micromechanical origins of globally emergent mechanical properties (as was done here) or supplement experimental studies by facilitating predictive design of gels with desired mechanical traits, based on controllable inputs. Nonetheless, this iteration of the model may be improved upon in several ways.

Features such as polydispersity, variability in the local mixing parameter, rate-dependent effects of solvent transport, and inclusion of reversible bonds are all compatible with this model and may be incorporated in future iterations. For example, the current model assumes a constant Flory parameter despite the demonstrable effects of both temperature and solute concentration on this statistical value (Bolhuis et al., 2001; Egorov, 2004; Huissmann et al., 2009; Jusufi et al., 1999; Krakoviack et al., 2003; Likos, 2001; Majka and Góra, 2014). While treating χ as a constant did not affect agreement between the model's predicted mechanical properties and those of experimental results for gels in theta solvent, solute-solvent interactions may play a more potent effect on the damage mechanics of gels in poor solvent or containing local pockets of effectively poor solvent quality. In such systems, we hypothesize that clustering of polymer chains may reduce their conformational degrees of freedom, thereby increasing their stored free energy and reducing the effective crosslink separation or network stretch at which chains begin to rupture. In gels with dynamic bonds, poor solvent may also increase the effective bond dissociation rate per (Eyring, 1935). In future work, we may incorporate these physics via another layer of the Eulerian mesh that tracks χ as a function of solute concentration. However, this addition is contingent on *a priori* knowledge of the $\chi - \phi$ relationship, which likely requires further molecular-scale investigation.

Another pertinent effect to consider is dissipation due to entanglement. Entanglements are ubiquitously hypothesized to play a part in the viscoelastic response of gels, particularly gels with high polydispersity (e.g., poly(acrylamide)) or chain length (Kavanagh and Ross-Murphy, 1998). Researchers such as Masubuchi et al. (2001) have previously introduced coarse-grained models in which entanglements are captured as slip links through which the passage of polymer depends on the entropic tension and density gradients of the chains on either side. Notably, this introduces sliding friction and dissipation that likely depend on the modes of entanglement. Yet, it remains unclear how to quantify the types and relative fractions of said modes experimentally. Therefore - inspired by Masubuchi et al. (2001) - in future work we will incorporate slip links into an iteration of this framework to instead model slide-ring gels whose crosslink characteristics (e.g., density and distribution) may be tuned and characterized empirically (Dikshit and Bruns, 2021), or inferred via continuum approaches (Vernerey and Lamont, 2021). More immediately, this iteration of the model will be improved by accounting for rate-dependent poroelastic effects and dynamic bonds. The former will be introduced and mediated by mesh-size-dependent transport of solvent through Darcy's law and incorporation of viscous drag (Hong et al., 2009, 2008; Mattern et al., 2008). This will allow for investigation of dynamic loading rates and time-dependent swelling inhomogeneity. Rate-dependence is also highly influenced by inclusion of reversible bonds, which imbue networks with viscous response and the ability to relax. In forthcoming work we incorporate reversible, telechelic bonds to investigate and predictively tune the properties of covalently adaptable networks that have potential applications as extracellular scaffolds in osteochondral tissue engineering (Akalp et al., 2016; Richardson et al., 2019; Vernerey, 2016). For gels containing such reversible bonds, any *a priori* knowledge about initial topology quickly loses significance as the networks reconfigure, particularly during applied loading. Therefore, methods that relate local crosslink distribution to underlying first-order physics are of great importance (Dhote and Vernerey, 2014; Sridhar et al., 2017).

Declaration of Competing Interest

The authors declare that they have no known competing financial interests or personal relationships that could have appeared to influence the work reported in this paper.

Acknowledgments

F.J.V. gratefully acknowledges the support of the National Science Foundation (NSF) under award no. 2029699. This content is solely the responsibility of the authors and does not necessarily represent the official views of NSF.

Appendix A. Domain size convergence study

To determine an appropriate RVE size, 10 kDa tetra-functional networks of $\mathcal{N} \in \{100, 225, 400, 625, 900\}$ nodes were generated, swelled, and uniaxially extended in direction $\boldsymbol{e}_2$ through the chronological processes described in Section 3. These networks correspond to approximately 10, 15, 20, 35, and 30 nodes per RVE edge, respectively. Strain was introduced at a constant strain rate (with traction free side boundaries) to a maximum stretch of $\lambda = 4$. Ten *in silico* experiments were conducted for each domain size and the ensemble averaged stress-stretch relations are depicted in Fig. A.1. It is clear from Fig. A.1 that, while networks containing $\mathcal{N} \in 100, 225$ nodes behaved more softly, no significant difference in mechanical response occurs between RVEs containing $\mathcal{N} \in \{400, 625, 900\}$. Therefore, all studies in this work are carried out with $\mathcal{N} = 400$ nodes. In addition, we ensure that the domain size always exceeds L by a factor greater than two so that single chains cannot span opposing periodic boundaries of the RVE.

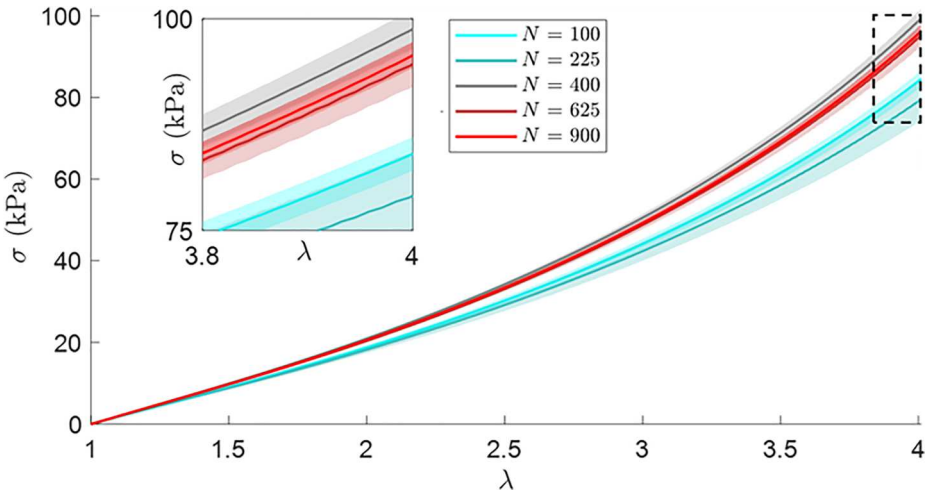

Fig. A.1. Domain size convergence of stress-stretch. The stress responses of RVEs containing $\mathcal{N} \in \{100, 225, 400, 625, 900\}$ nodes are displayed for networks stretched to $\lambda = 4$. The inset displays the stress-stretch response of the region outlined by the dashed box ($\lambda \in [3.8, 4]$ and $\sigma \in [75, 100]$ kPa) to emphasize overlap for the cases of $\mathcal{N} \in \{400, 625, 900\}$.

Appendix B. Length scale and as-prepared concentration calibration

Given the nearly monodisperse nature of star-shaped PEG macromers (Sakai, 2014; Sakai et al., 2008) one may compute the effective molar mass per arm as M_w/f. Given ethylene oxide's molar mass ($M_{eg} = 44.05$ kg mol^{-1}), then the number of mers in an arm is $N_{arm} = M_{eg}f/M_w$. We take the length of a single PEG mer as 3.9 Å and treat each Kuhn segment as two mers (Liese et al., 2017) so that $N = N_{arm}/2$ and $b = 7.8$ Å. In the numerical framework, we set the normalized length scale as $L = Nb = 1$. As such, conversion between SI units and the numerical frameworks length scale is given by the conversion:

$$1 = \frac{M_{eg}}{M_w} fb \tag{B.1}$$

The as-prepared polymer fraction is computed as the total polymer volume (or area in 2D), A_{star}, divided by the RVE size, A_{RVE}:

$$\phi = \frac{A_{star}}{A_{RVE}} \tag{B.2}$$

This as-prepared concentration is normalized by the overlap volume fraction, which is taken as:

$$\phi_{ol} = \frac{A_{star}}{\pi R_g^2} \tag{B.3}$$

where R_g is the radius of gyration for a single star-shaped macromer and is estimated using (Lue and Kiselev, 2002):

$$R_g^2 \sim N f^{1/2} b^2 \tag{B.4}$$

for low functionality star-polymers in theta solvent. Combining ((B.2)–(B.4)), one may write the normalized, as-prepared solute volume fraction as:

$$\phi^* = \frac{\pi N f^{1/2} b^2}{A_{RVE}} \tag{B.5}$$

Ergo, ϕ^* is controlled in the framework by tuning A_{RVE}.

Appendix C. The extensile bulk modulus of a gel's polymer network

A critical consideration in fitting the analytical model to our numerical results is what form the bulk modulus of the polymer network, κ, takes and whether it evolves with the swelling ratio, J. Note that this is here defined as the extensile bulk modulus of solely the polymer network and does not constitute the overall bulk modulus of the gel, thus κ in this section is decoupled from the osmotic pressure of mixing. Furthermore, volume exclusion effects on κ are not considered, as these primarily matter for gels at high polymer concentrations or those undergoing compressive loading (Drozdov and Christiansen, 2020). Fundamentally, the bulk modulus of a freely swelling gel's polymer network may be defined as its resistance to volumetric change through $\kappa = \partial\sigma^h/\partial V$. Since PEG-based gels (with $M_w > 10$ kDa) in theta solvent generally have polymer volume fractions on the order of $\phi \sim 0.01 - 0.1$ (Akagi et al., 2010; Lange et al., 2011; Matsunaga

et al., 2009b), and entanglements have been shown to play little part in the swelling dynamics of these relatively homogenous gels (Matsunaga et al., 2009b; Sugimura et al., 2013), we may neglect the effects of steric interactions between chains and crosslinks during swelling. Furthermore, assuming steady state swelling and that the gel is submersed in a sufficiently large solvent bath at thermodynamic equilibrium with its surroundings, then mixing (and therefore swelling) is not limited by solvent availability or transport and is therefore only resisted by the elastic tension of the polymer chains. As such, κ during swelling may be interpreted as entirely dependent on the elastic network properties.

The first component of the virial stress is synonymous with Cauchy stress for non-inertial networks and given by Eq. (26). For linear springs, $f = Kr$, and K is the stiffness of a single chain, $K = 3k_bT/r_0^2$, V is the material volume ($V = V_0J$), and $V_0 = \mathcal{N}/c_0$ where $\mathcal{N}$ is the number of chains that exists in the domain ($\in \Omega$), c_0 is the dry concentration of chains, and $r_0 = \sqrt{N}b$ is initial mean end-to-end separation for ideal chains (i.e., in theta solvent). As such, Eq. (26) may be rewritten as:

$$\boldsymbol{\sigma}_v = \frac{c_0}{2\mathcal{N}J}\left(\frac{3k_bT}{Nb^2}\right)\sum_{\Omega}\boldsymbol{r}\otimes\boldsymbol{r} \tag{C.1}$$

Substituting the definition of $\boldsymbol{r}$ to rewrite (C.1) as a function of chain stretch, $\boldsymbol{\lambda}$ ($\boldsymbol{r} = r_0\boldsymbol{\lambda} = \boldsymbol{\lambda}\sqrt{N}b$), gives:

$$\boldsymbol{\sigma}_v = \frac{3k_bTc_0}{2\mathcal{N}J}\sum_{\Omega}\boldsymbol{\lambda}\otimes\boldsymbol{\lambda} \tag{C.2}$$

From (C.2), the hydrostatic component of stress may be written in 2D as:

$$\sigma^h = \frac{3k_bTc_0}{4\mathcal{N}J}\,\mathrm{tr}\left(\sum_{\Omega}\boldsymbol{\lambda}\otimes\boldsymbol{\lambda}\right) \tag{C.3}$$

where for the case of isotropic swelling under the affine assumption:

$$\mathrm{tr}\left(\sum_{\mathcal{N}}\boldsymbol{\lambda}\otimes\boldsymbol{\lambda}\right) = \mathcal{N}(\lambda_1\lambda_1 + \lambda_2\lambda_2) = 2\mathcal{N}\lambda^2 = 2\mathcal{N}J \tag{C.4}$$

Substituting this definition into (C.3), gives:

$$\sigma^h = \frac{3}{2}k_bTc_0 \tag{C.5}$$

Thus, $\kappa = \partial\sigma^h/\partial J = 0$, at least at high volumetric strains for which the invoked assumptions apply (i.e., no polymer-polymer volume exclusion interactions).

Appendix D. Extended 40k tetra- and 80k octa-PEG gel data

To demonstrate that the trends discussed in Section 5.1 (with regards to short-armed tetra- and octa-functional networks) also apply the networks with longer chain lengths, we provide analogous figures to Figs. 13, 14 and 16.

Figs. (D1–D3).

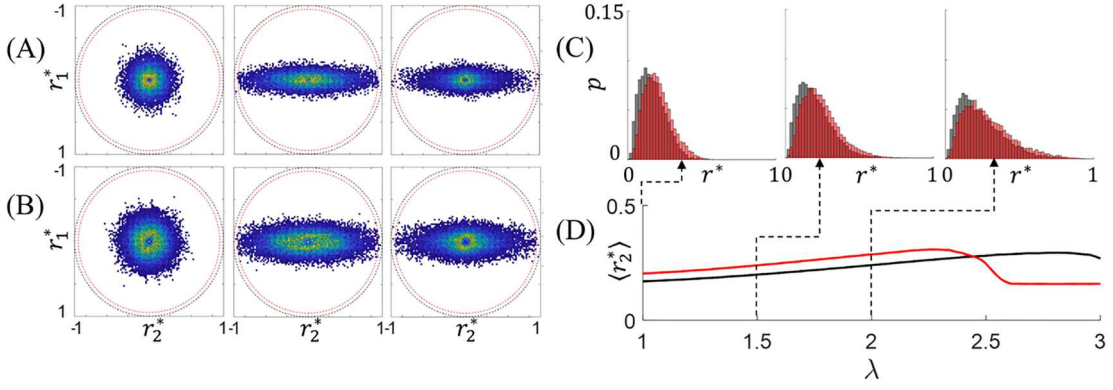

Fig. D.1. Chain distribution functions of gels with L = 177 nm and different functionalities. (A) The joint PDF of r^* is shown for the ensemble of ten 40k tetra-PEG gels at $\lambda = 1$ (left), the measured yield stretch $\lambda = 2.80$ (center), and the measured failure stretch $\lambda = 3.25$ (right). (B) The joint PDF of r^* is shown for the ensemble of ten 80k octa-PEG gels at $\lambda = 1$ (left), the measured yield stretch $\lambda = 2.36$ (center), and the measured failure stretch $\lambda = 2.52$ (right). (A,B) The extensile direction, $\boldsymbol{e}_2$, is oriented horizontally. Dashed black circles indicate the chain contour length, while dashed red circles represent the deterministic scission length for chains. (C) The radial PDFs of r^* are shown for the 10k tetra- and 20k octa-PEG gels as black and red histograms, respectively. For direct comparison, these histograms are depicted at $\lambda = 0$ (left), $\lambda = 1.5$ (center), and $\lambda = 2.0$. Again, the chains in these two networks have the same contour length. (D) The average component of normalized chain end-to-end length in the principal direction of extension is plotted with respect to stretch. End-to-end lengths are normalized as $r^* = r/L$ such that $r^* \geq 0.95$ is not permitted.

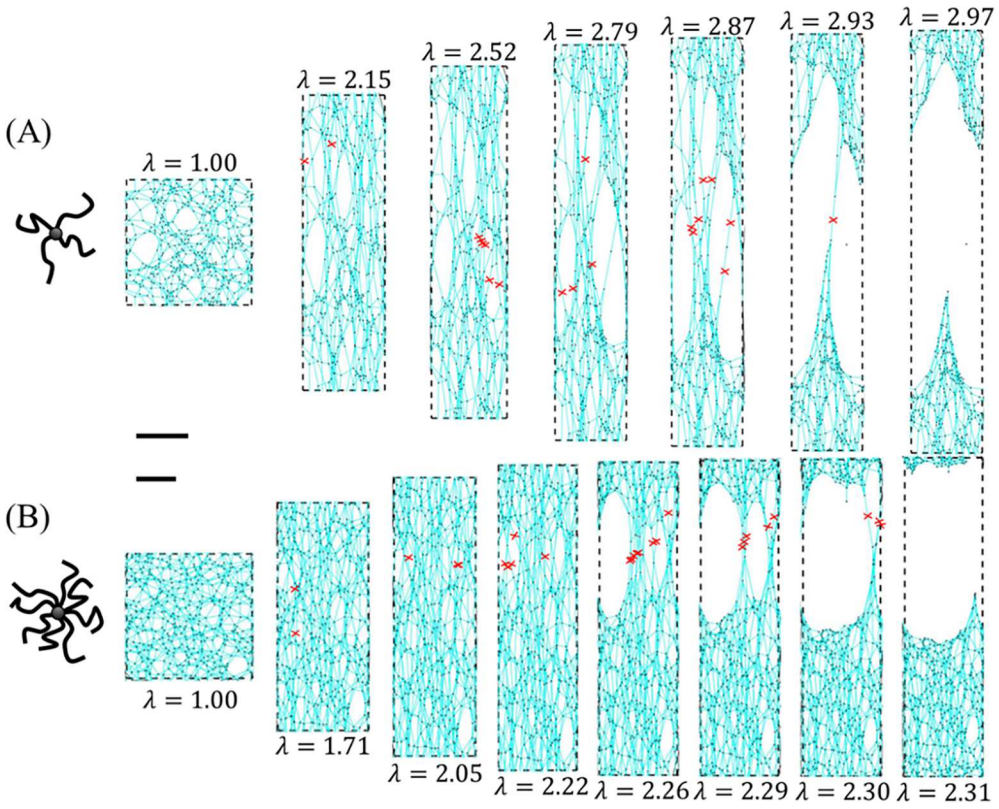

Fig. D.2. Fracture of gels with of gels with L = 177 nm and different functionalities. (A) A schematic of a tetra-functional macromer is depicted, alongside snapshots of a simulated 40k tetra-PEG gel as it undergoes uniaxial extension. (B) A schematic of an octa-functional macromer is depicted, alongside snapshots of a simulated 80k octa-PEG gel as it undergoes uniaxial extension. The sizes of the gel snapshots are indicated by their respective scale bars, each representing L. Red crosses in the gel snapshots demark which chains rupture before the next displayed snapshot.

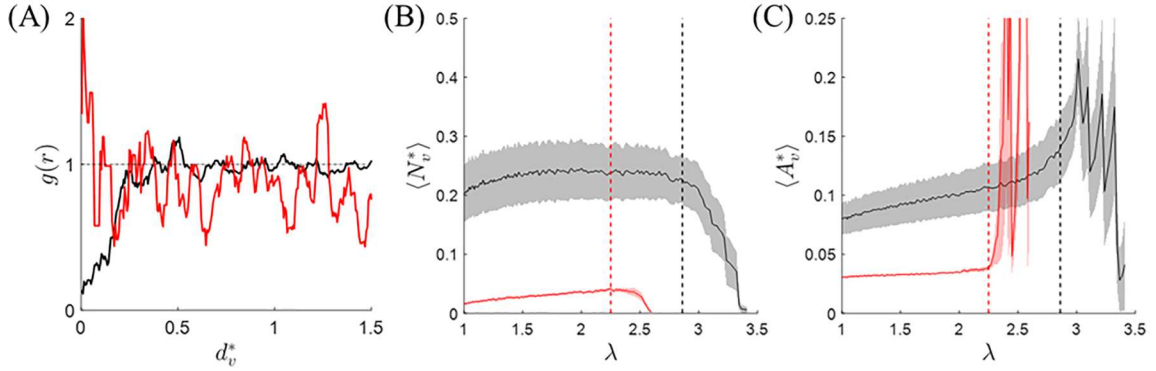

Fig. D.3. Void characteristics of gels with L = 177 nm and different functionalities. (A) The RDFs of ensembles of ten 40k tetra-PEG (black) and ten 80k octa-PEG (red) gels' void centroids are displayed at $\lambda = 1$. Unlike for the short-armed networks, there is no detectable correlation scale for voids the octa-functional networks. The distance between void centroids is normalized as $d_v^* = d_v/L$. (B) The average number of voids per macromer is plotted with respect to stretch. (C) The average void area (normalized as $A_v^* = A_v/\pi L^2$) is plotted with respect to stretch. (B,C) Shaded regions represent S.E. of the mean. The vertical dotted lines denote the approximate stretches at which bond rupture events became significant ($\lambda \approx 2.85$ - black, $\lambda \approx 2.25$ - red).

References

Ahlawat, V., Rajput, S.S., Patil, S., 2021. Elasticity of single flexible polymer chains in good and poor solvents. Polymer 230, 124031. https://doi.org/10.1016/j.polymer.2021.124031.

Akagi, Y., Matsunaga, T., Shibayama, M., Chung, U., Sakai, T., 2010. Evaluation of topological defects in Tetra-PEG Gels. Macromolecules 43, 488–493. https://doi.org/10.1021/ma9019009.

Akalp, U.J., Bryant, S.J., Vernerey, F., 2016. Tuning tissue growth with scaffold degradation in enzyme-sensitive hydrogels: a mathematical model. Soft Matter 12, 7505–7520. https://doi.org/10.1039/C6SM00583G.
Asai, M., Katashima, T., Chung, U., Sakai, T., Shibayama, M., 2013. Correlation between local and global inhomogeneities of chemical gels. Macromolecules 46, 9772–9781. https://doi.org/10.1021/ma400486h.
Bell, G.I., 1978. Models for the specific adhesion of cells to cells. Science 200, 618–627.
Bergström, J.S., Boyce, M.C., 2001. Deformation of elastomeric networks: relation between molecular level deformation and classical statistical mechanics models of rubber elasticity. Macromolecules 34, 614–626. https://doi.org/10.1021/ma0007942.
Birshtein, T.M., Zhulina, E.B., 1990. Scaling theory of supermolecular structures in block copolymer-solvent systems: 2. Supercrystalline structures. Polymer 31, 1312–1320. https://doi.org/10.1016/0032-3861(90)90223-L.
Birshtein, T.M., Zhulina, E.B., 1984. Conformations of star-branched macromolecules. Polymer 25, 1453–1461. https://doi.org/10.1016/0032-3861(84)90109-5.
Bolhuis, P.G., Louis, A.A., Hansen, J.P., Meijer, E.J., 2001. Accurate effective pair potentials for polymer solutions. J. Chem. Phys. 114, 4296–4311. https://doi.org/10.1063/1.1344606.
Chaudhuri, O., Gu, L., Klumpers, D., Darnell, M., Bencherif, S.A., Weaver, J.C., Huebsch, N., Lee, H.P., Lippens, E., Duda, G.N., Mooney, D.J., 2016. Hydrogels with tunable stress relaxation regulate stem cell fate and activity. Nat. Mater. 15, 326–334. https://doi.org/10.1038/nmat4489.
Chen, C., Wang, Z., Suo, Z., 2017. Flaw sensitivity of highly stretchable materials. Extrem. Mech. Lett. 10, 50–57. https://doi.org/10.1016/j.eml.2016.10.002. Filling Gaps in Material Property Space: IUTAM Symposium.
Choi, B., Park, K.S., Kim, J.H., Ko, K.W., Kim, J.S., Han, D.K., Lee, S.H., 2016. Stiffness of hydrogels regulates cellular reprogramming efficiency through mesenchymal-to-epithelial transition and stemness markers. Macromol. Biosci. 16, 199–206. https://doi.org/10.1002/mabi.201500273.
Chung, J.W., Roos, A., De Hosson, J.T.M., van der Giessen, E., 1996. Fracture of disordered three-dimensional spring networks: a computer simulation methodology. Phys. Rev. B 54, 15094–15100. https://doi.org/10.1103/PhysRevB.54.15094.
Cohen, A., 1991. A Padé approximant to the inverse Langevin function. Rheol. Acta 30, 270–273. https://doi.org/10.1007/BF00366640.
Daoud, M., Cotton, J.P., 1982. Star shaped polymers : a model for the conformation and its concentration dependence. J. Phys. Fr. 43, 531–538. https://doi.org/10.1051/jphys:01982004303053100.
Dhote, V., Vernerey, F.J., 2014. Mathematical model of the role of degradation on matrix development in hydrogel scaffold. Biomech. Model. Mechanobiol. 13, 167–183. https://doi.org/10.1007/s10237-013-0493-0.
Dikshit, K., Bruns, C.J., 2021. Post-synthesis modification of slide-ring gels for thermal and mechanical reconfiguration. Soft Matter 17, 5248–5257. https://doi.org/10.1039/D0SM02260H.
Doi, M., 2013. Soft Matter Physics. OUP, Oxford.
Drozdov, A.D., Christiansen, J., 2020. Tension-compression asymmetry in the mechanical response of hydrogels. J. Mech. Behav. Biomed. Mater. 110, 103851 https://doi.org/10.1016/j.jmbbm.2020.103851.
Egorov, S.A., 2004. Effect of repulsive and attractive interactions on depletion forces in colloidal suspensions: a density functional theory treatment. Phys. Rev. E 70, 031402. https://doi.org/10.1103/PhysRevE.70.031402.
Elbanna, A.E., Carlson, J.M., 2013. Dynamics of polymer molecules with sacrificial bond and hidden length systems: towards a physically-based mesoscopic constitutive law. PLOS ONE 8, e56118. https://doi.org/10.1371/journal.pone.0056118.
Eyring, H., 1935. The activated complex and the absolute rate of chemical reactions. Chem. Rev. 17, 65–77. https://doi.org/10.1021/cr60056a006.
Fantner, G.E., Hassenkam, T., Kindt, J.H., Weaver, J.C., Birkedal, H., Pechenik, L., Cutroni, J.A., Cidade, G.A.G., Stucky, G.D., Morse, D.E., Hansma, P.K., 2005. Sacrificial bonds and hidden length dissipate energy as mineralized fibrils separate during bone fracture. Nat. Mater. 4, 612–616. https://doi.org/10.1038/nmat1428.
Flory, P.J., 1985. Molecular theory of rubber elasticity. Polym. J. 17, 1–12. https://doi.org/10.1295/polymj.17.1.
Flory, P.J., Fisk, S., 1966. Effect of volume exclusion on the dimensions of polymer chains. J. Chem. Phys. 44, 2243–2248. https://doi.org/10.1063/1.1727029.
Flory, P.J., Rehner, J., 1943a. Statistical mechanics of cross-linked polymer networks I. Rubberlike elasticity. J Chem. Phys. 11, 512–520. https://doi.org/10.1063/1.1723791.
Flory, P.J., Rehner, J., 1943b. Statistical mechanics of cross-linked polymer networks II. Swelling. J. Chem. Phys. 11, 521–526. https://doi.org/10.1063/1.1723792.
Gianneli, M., Beines, P.W., Roskamp, R.F., Koynov, K., Fytas, G., Knoll, W., 2007. Local and global dynamics of transient polymer networks and swollen gels anchored on solid surfaces. J. Phys. Chem. C 111, 13205–13211. https://doi.org/10.1021/jp0728959.
Hebbeker, P., Plamper, F.A., Schneider, S., 2018. Aggregation of star polymers: complexation versus segregation. Macromol. Theory Simul. 27, 1800033 https://doi.org/10.1002/mats.201800033.
Hong, W., Liu, Z., Suo, Z., 2009. Inhomogeneous swelling of a gel in equilibrium with a solvent and mechanical load. Int. J. Solids Struct. 46, 3282–3289. https://doi.org/10.1016/j.ijsolstr.2009.04.022.
Hong, W., Zhao, X., Zhou, J., Suo, Z., 2008. A theory of coupled diffusion and large deformation in polymeric gels. J. Mech. Phys. Solids 56, 1779–1793. https://doi.org/10.1016/j.jmps.2007.11.010.
Horkay, F., Lin, D.C., 2009. Mapping the local osmotic modulus of polymer gels. Langmuir 25, 8735–8741. https://doi.org/10.1021/la900103j.
Horkay, F., Nishi, K., Shibayama, M., 2017. Decisive test of the ideal behavior of tetra-PEG gels. J. Chem. Phys. 146, 164905 https://doi.org/10.1063/1.4982253.
Hosein, I.D., Lee, S.H., Liddell, C.M., 2010. Dimer-based three-dimensional photonic crystals. Adv. Funct. Mater. 20, 3085–3091. https://doi.org/10.1002/adfm.201000134.
Hsu, H.P., Nadler, W., Grassberger, P., 2004. Scaling of star polymers with 1−80 Arms. Macromolecules 37, 4658–4663. https://doi.org/10.1021/ma0355958.
Huissmann, S., Blaak, R., Likos, C.N., 2009. Star polymers in solvents of varying quality. Macromolecules 42, 2806–2816. https://doi.org/10.1021/ma8023359.
Jangizehi, A., Schmid, F., Besenius, P., Kremer, K., Seiffert, S., 2020. Defects and defect engineering in soft matter. Soft Matter 16, 10809–10859. https://doi.org/10.1039/D0SM01371D.
Johner, A., Lee, N.K., 2018. The Daoud and Cotton blob model and the interaction of star-shaped polymers. Eur. Phys. J. E 41, 88. https://doi.org/10.1140/epje/i2018-11698-3.
Jusufi, A., Watzlawek, M., Löwen, H., 1999. Effective interaction between star polymers. Macromolecules 32, 4470–4473. https://doi.org/10.1021/ma981844u.
Kavanagh, G.M., Ross-Murphy, S.B., 1998. Rheological characterisation of polymer gels. Prog. Polym. Sci. 23, 533–562. https://doi.org/10.1016/S0079-6700(97)00047-6.
Khoiroh, I., Lee, S.Y., Pirdashti, M., Lee, M.J., 2020. Insight into structural properties of polyethylene glycol monolaurate in water and alcohols from molecular dynamics studies. RSC Adv. 10, 21760–21771. https://doi.org/10.1039/C9RA09688D.
Kienberger, F., Pastushenko, V.P., Kada, G., Gruber, H.J., Riener, C., Schindler, H., Hinterdorfer, P., 2000. Static and dynamical properties of single poly(Ethylene glycol) molecules investigated by force spectroscopy. Single Mol. 1, 123–128. https://doi.org/10.1002/1438-5171(200006)1:2<123::AID-SIMO123>3.0.CO;2-3.
Kothari, K., Hu, Y., Gupta, S., Elbanna, A., 2018. Mechanical response of two-dimensional polymer networks: role of topology, rate dependence, and damage accumulation. J. Appl. Mech. 85 https://doi.org/10.1115/1.4038883.
Krakoviack, V., Hansen, J.P., Louis, A.A., 2003. Influence of solvent quality on effective pair potentials between polymers in solution. Phys. Rev. E 67, 041801. https://doi.org/10.1103/PhysRevE.67.041801.
Lamont, S.C., Mulderrig, J., Bouklas, N., Vernerey, F.J., 2021. Rate-dependent damage mechanics of polymer networks with reversible bonds. Macromolecules 54, 10801–10813. https://doi.org/10.1021/acs.macromol.1c01943.
Lange, F., Schwenke, K., Kurakazu, M., Akagi, Y., Chung, U., Lang, M., Sommer, J.U., Sakai, T., Saalwächter, K., 2011. Connectivity and structural defects in model hydrogels: a combined proton NMR and Monte Carlo simulation study. Macromolecules 44, 9666–9674. https://doi.org/10.1021/ma201847v.
Lee, H., Larson, R.G., 2009. Molecular dynamics study of the structure and interparticle interactions of polyethylene glycol-conjugated PAMAM dendrimers. J. Phys. Chem. B 113, 13202–13207. https://doi.org/10.1021/jp906497e.

Li, X., Cui, K., Kurokawa, T., Ye, Y.N., Sun, T.L., Yu, C., Creton, C., Gong, J.P., 2021. Effect of mesoscale phase contrast on fatigue-delaying behavior of self-healing hydrogels. Sci. Adv. 7, eabe8210. https://doi.org/10.1126/sciadv.abe8210.
Li, X., Cui, K., Sun, T.L., Meng, L., Yu, C., Li, L., Creton, C., Kurokawa, T., Gong, J.P., 2020. Mesoscale bicontinuous networks in self-healing hydrogels delay fatigue fracture. PNAS 117, 7606–7612. https://doi.org/10.1073/pnas.2000189117.
Lieou, C.K.C., Elbanna, A.E., Carlson, J.M., 2013. Sacrificial bonds and hidden length in biomaterials: a kinetic constitutive description of strength and toughness in bone. Phys. Rev. E 88, 012703. https://doi.org/10.1103/PhysRevE.88.012703.
Liese, S., Gensler, M., Krysiak, S., Schwarzl, R., Achazi, A., Paulus, B., Hugel, T., Rabe, J.P., Netz, R.R., 2017. Hydration effects turn a highly stretched polymer from an entropic into an energetic spring. ACS Nano 11, 702–712. https://doi.org/10.1021/acsnano.6b07071.
Likos, C.N., 2001. Effective interactions in soft condensed matter physics. Phys. Rep. 348, 267–439. https://doi.org/10.1016/S0370-1573(00)00141-1.
Long, R., Mayumi, K., Creton, C., Narita, T., Hui, C.Y., 2014. Time dependent behavior of a dual cross-link self-healing gel: theory and experiments. Macromolecules 47, 7243–7250. https://doi.org/10.1021/ma501290h.
Lue, L., Kiselev, S.B., 2002. Star polymers in good solvents from dilute to concentrated regimes: crossover approach. Condens. Matter Phys. 5, 73. https://doi.org/10.5488/CMP.5.1.73.
Majka, M., Góra, P.F., 2014. Analytical theory of effective interactions in binary colloidal systems of soft particles. Phys. Rev. E 90, 032303. https://doi.org/10.1103/PhysRevE.90.032303.
Masubuchi, Y., Takimoto, J.I., Koyama, K., Ianniruberto, G., Marrucci, G., Greco, F., 2001. Brownian simulations of a network of reptating primitive chains. J. Chem. Phys. 115, 4387–4394. https://doi.org/10.1063/1.1389858.
Matsunaga, T., Sakai, T., Akagi, Y., Chung, U., Shibayama, M., 2009a. SANS and SLS studies on tetra-arm PEG gels in as-prepared and swollen states. Macromolecules 42, 6245–6252. https://doi.org/10.1021/ma901013q.
Matsunaga, T., Sakai, T., Akagi, Y., Chung, U., Shibayama, M., 2009b. Structure Characterization of tetra-PEG gel by small-angle neutron scattering. Macromolecules 42, 1344–1351. https://doi.org/10.1021/ma802280n.
Mattern, K.J., Nakornchai, C., Deen, W.M., 2008. Darcy permeability of agarose-glycosaminoglycan gels analyzed using fiber-mixture and Donnan models. Biophys. J. 95, 648–656. https://doi.org/10.1529/biophysj.107.127316.
Moerman, K.M., Fereidoonnezhad, B., McGarry, J.P., 2020. Novel hyperelastic models for large volumetric deformations. Int. J. Solids Struct. 193-194, 474–491. https://doi.org/10.1016/j.ijsolstr.2020.01.019.
Mohanty, P.S., Paloli, D., Crassous, J.J., Zaccarelli, E., Schurtenberger, P., 2014. Effective interactions between soft-repulsive colloids: experiments, theory, and simulations. J. Chem. Phys. 140, 094901 https://doi.org/10.1063/1.4866644.
Narita, T., Mayumi, K., Ducouret, G., Hébraud, P., 2013. Viscoelastic properties of poly(vinyl alcohol) hydrogels having permanent and transient cross-links studied by microrheology, classical rheometry, and dynamic light scattering. Macromolecules 46, 4174–4183. https://doi.org/10.1021/ma400600f.
Oesterhelt, F., Rief, M., Gaub, H.E., 1999. Single molecule force spectroscopy by AFM indicates helical structure of poly(ethylene-glycol) in water. New J. Phys. 1, 6. https://doi.org/10.1088/1367-2630/1/1/006.
Ogden, R.W., Hill, R., 1972. Large deformation isotropic elasticity: on the correlation of theory and experiment for compressible rubberlike solids. Proc. R. Soc. Lond. A Math. Phys. Sci. 328, 567–583. https://doi.org/10.1098/rspa.1972.0096.
Padding, J.T., Briels, W.J., 2014. Momentum conserving Brownian dynamics propagator for complex soft matter fluids. J. Chem. Phys. 141, 244108 https://doi.org/10.1063/1.4904315.
Picu, R.C., 2011. Mechanics of random fiber networks—a review. Soft Matter 7, 6768–6785. https://doi.org/10.1039/C1SM05022B.
Richardson, B.M., Wilcox, D.G., Randolph, M.A., Anseth, K.S., 2019. Hydrazone covalent adaptable networks modulate extracellular matrix deposition for cartilage tissue engineering. Acta Biomater. 83, 71–82. https://doi.org/10.1016/j.actbio.2018.11.014.
Riley, E.K., Watson, C.M.L., 2014. Slab photonic crystals with dimer cylinder bases. J. Opt. Soc. Am. B JOSA B 31, 2084–2094. https://doi.org/10.1364/JOSAB.31.002084.
Sakai, T., 2014. Experimental verification of homogeneity in polymer gels. Polym. J. 46, 517–523. https://doi.org/10.1038/pj.2014.28.
Sakai, T., Akagi, Y., Matsunaga, T., Kurakazu, M., Chung, U., Shibayama, M., 2010. Highly elastic and deformable hydrogel formed from tetra-arm polymers. Macromol. Rapid Commun. 31, 1954–1959. https://doi.org/10.1002/marc.201000286.
Sakai, T., Matsunaga, T., Yamamoto, Y., Ito, C., Yoshida, R., Suzuki, S., Sasaki, N., Shibayama, M., Chung, U., 2008. Design and fabrication of a high-strength hydrogel with ideally homogeneous network structure from tetrahedron-like macromonomers. Macromolecules 41, 5379–5384. https://doi.org/10.1021/ma800476x.
Salari, A., Karmozdi, M., Maddahian, R., Firoozabadi, B., 2013. Analytical study of single particle tracking in both free and forced vortices. Sci. Iran. 20, 351–358. https://doi.org/10.1016/j.scient.2013.02.011.
Sanoja, G.E., Morelle, X.P., Comtet, J., Yeh, C.J., Ciccotti, M., Creton, C., 2021. Why is mechanical fatigue different from toughness in elastomers? The role of damage by polymer chain scission. Science Advances 7, eabg9410. https://doi.org/10.1126/sciadv.abg9410.
Schultz, K.M., Baldwin, A.D., Kiick, K.L., Furst, E.M., 2009. Gelation of covalently cross-linked PEG−heparin hydrogels. Macromolecules 42, 5310–5316. https://doi.org/10.1021/ma900766u.
Schwenke, K., Lang, M., Sommer, J.U., 2011. On the structure of star-polymer networks. Macromolecules 44, 9464–9472. https://doi.org/10.1021/ma202022q.
Shibayama, M., Li, X., Sakai, T., 2019. Precision polymer network science with tetra-PEG gels—a decade history and future. Colloid Polym. Sci. 297, 1–12. https://doi.org/10.1007/s00396-018-4423-7.
Soffer, S.N., Vázquez, A., 2005. Network clustering coefficient without degree-correlation biases. Phys. Rev. E 71, 057101. https://doi.org/10.1103/PhysRevE.71.057101.
Sridhar, S.L.C., Schneider, M., Chu, S., Roucy, G., de, J., Bryant, S.J., Vernerey, F., 2017. Heterogeneity is key to hydrogel-based cartilage tissue regeneration. Soft Matter 13, 4841–4855. https://doi.org/10.1039/C7SM00423K.
Stukalin, E.B., Cai, L.H., Kumar, N.A., Leibler, L., Rubinstein, M., 2013. Self-healing of unentangled polymer networks with reversible bonds. Macromolecules 46, 7525–7541. https://doi.org/10.1021/ma401111n.
Sugimura, A., Asai, M., Matsunaga, T., Akagi, Y., Sakai, T., Noguchi, H., Shibayama, M., 2013. Mechanical properties of a polymer network of tetra-PEG gel. Polym. J. 45, 300–306. https://doi.org/10.1038/pj.2012.149.
Sukumar, V.S., Lopina, S.T., 2002. Network model for the swelling properties of end-linked linear and star poly(ethylene oxide) hydrogels. Macromolecules 35, 10189–10192. https://doi.org/10.1021/ma0213753.
Sun, G., Zhang, X.Z., Chu, C.C., 2008. Effect of the molecular weight of polyethylene glycol (PEG) on the properties of chitosan-PEG-poly(N-isopropylacrylamide) hydrogels. J. Mater. Sci. Mater. Med. 19, 2865–2872. https://doi.org/10.1007/s10856-008-3410-9.
Tanaka, T., Fillmore, D.J., 1979. Kinetics of swelling of gels. J. Chem. Phys. 70, 1214–1218. https://doi.org/10.1063/1.437602.
Temenoff, J.S., Athanasiou, K.A., Lebaron, R.G., Mikos, A.G., 2002. Effect of poly(ethylene glycol) molecular weight on tensile and swelling properties of oligo(poly(ethylene glycol) fumarate) hydrogels for cartilage tissue engineering. J. Biomed. Mater. Res. 59, 429–437. https://doi.org/10.1002/jbm.1259.
Vernerey, F.J., 2016. A mixture approach to investigate interstitial growth in engineering scaffolds. Biomech. Model. Mechanobiol. 15, 259–278. https://doi.org/10.1007/s10237-015-0684-y.
Vernerey, F.J., Brighenti, R., Long, R., Shen, T., 2018. Statistical damage mechanics of polymer networks. Macromolecules 51, 6609–6622. https://doi.org/10.1021/acs.macromol.8b01052.
Vernerey, F.J., Lamont, S., 2021. Transient mechanics of slide-ring networks: a continuum model. J. Mech. Phys. Solids 146, 104212. https://doi.org/10.1016/j.jmps.2020.104212.
Vernerey, F.J., Long, R., Brighenti, R., 2017. A statistically-based continuum theory for polymers with transient networks. J. Mech. Phys. Solids 107, 1–20. https://doi.org/10.1016/j.jmps.2017.05.016.
Wagner, R.J., Hobbs, E., Vernerey, F.J., 2021. A network model of transient polymers: exploring the micromechanics of nonlinear viscoelasticity. Soft Matter. https://doi.org/10.1039/D1SM00753J.

Wang, E., Escobedo, F., 2017. Swelling and tensile properties of tetra-polyethylene glycol via coarse-grained molecular models. Macromol. Theory Simul. 26, 1600098 https://doi.org/10.1002/mats.201600098.
Wang, L., Lei, K., Li, Z., Wang, X., Xiao, H., Zheng, Z., 2018. Tetra-PEG-based nano-enhanced hydrogel with excellent mechanical properties and multi-functions. Macromol. Mater. Eng. 303, 1800325 https://doi.org/10.1002/mame.201800325.
Watzlawek, M., Löwen, H., Likos, C.N., 1998. The anomalous structure factor of dense star polymer solutions. J. Phys. Condens. Matter 10, 8189–8205. https://doi.org/10.1088/0953-8984/10/37/007.
Yang, C., DelRio, F.W., Ma, H., Killaars, A.R., Basta, L.P., Kyburz, K.A., Anseth, K.S., 2016. Spatially patterned matrix elasticity directs stem cell fate. PNAS 113, E4439–E4445. https://doi.org/10.1073/pnas.1609731113.
Yang, C., Yin, T., Suo, Z., 2019. Polyacrylamide hydrogels. I. Network imperfection. J. Mech. Phys. Solids 131, 43–55. https://doi.org/10.1016/j.jmps.2019.06.018.
Zhang, A., Ling, J., Sun, Y., Fu, G., 2015. Three-dimensional molecular geometry of PEG hydrogels by an "expansion-contraction" method through Monte Carlo simulations. Chin. J. Polym. Sci. 33, 721–731. https://doi.org/10.1007/s10118-015-1620-4.